Corrosion Science 218 (2023) 111166

Contents lists available at ScienceDirect

Corrosion Science

journal homepage: www.elsevier.com/locate/corsci

Localized and stress corrosion cracking of sensitized Al-Mg-Sc-Zr alloy manufactured by laser powder bed fusion

Leticia Cabrera-Correa [a,b,c], Leandro González-Rovira [a,b,*], Adrián Ojeda-López [a,b,c], Juan de Dios López-Castro [a,b,c], F. Javier Botana [a,b]

[a] Departamento de Ciencia de los Materiales e Ingeniería Metalúrgica y Química Inorgánica, Universidad de Cádiz, Escuela Superior de Ingeniería, Puerto Real, Cádiz 11519, Spain
[b] IMEYMAT: Institute of Research on Electron Microscopy and Materials, Universidad de Cádiz, Spain
[c] Titania, Ensayos y Proyectos Industriales S.L. Ed. RETSE, nave 4, 11500 El Puerto de Santa María, Spain

ARTICLE INFO

Keywords:
A: aluminium
B: polarization
SEM
Weight loss
C: intergranular corrosion
Stress corrosion

ABSTRACT

The effect of thermal ageing at 150 ºC on the corrosion behaviour of Scalmalloy® (Al-Mg-Sc-Zr) alloy additively manufactured by laser powder bed fusion (LPBF) is reported for the first time. Samples before and after the thermal treatment exhibit similar results on cyclic polarisation curves, electrochemical impedance measurements in 3.5 wt% NaCl, and tensile and hardness tests. However, electron microscopy characterisation reveals that the application of this temperature for sufficient time causes most of the grain limits to be decorated by Al_3Mg_2 particles which in turn provokes the sensitization of the alloy to intergranular corrosion processes due to microgalvanic coupling.

1. Introduction

Metal additive manufacturing technologies allow manufacturing parts layer by layer from a three-dimensional digital model. Specifically, laser powder bed fusion (LPBF) technology is one of the most employed additive technologies for the manufacture of metallic parts. LPBF is finding an increasing field of application. The possibilities of using new designs, reducing the number of elements or reducing their weight attract the interest of strategic sectors such as aerospace. Within this sector, great attention has been paid in recent years to develop new high-strength aluminium alloys that can be processed by LPBF. This need is related to the fact that high tensile strength alloys (7xxx, 2xxx and 6xxx series) undergo solidification cracking when processed by LPBF [1–6]. As a result, there have been great advances in the development of new aluminium alloys studied in the literature [1–3].

In this context, APWORKS company developed Scalmalloy® aluminium alloy specifically to be processed using LPBF technology [7,8]. Scalmalloy® is an aluminium alloy that contains between 4.0 and 4.9 wt% Mg, in addition to Sc, Zr, Si and Mn among other minor alloying elements. Among those aluminium alloys that can currently be used with LPBF technology, Scalmalloy® is one of the alloys with the best mechanical properties [1,3,9], which are mainly related with fine grain size and the occurrence of $Al_3(Sc_{1-x},Zr_x)$ nanoprecipitates in the microstructure [10]. Therefore, the study of this alloy is a hot topic in the literature nowadays, being possible to find a growing number of works in which its mechanical properties [11–15], microstructure [16–19] or applications [20–24] are studied.

However, the employment of Scalmalloy® in critical aircraft structures is still incipient. In order to promote the use of this alloy, it is essential to have more information related to the in-service behaviour of parts manufactured using LPBF. In this sense, the scarcity of works related to the study of the corrosion behaviour of this material is especially noticeable. With the aim of filling this gap, our group recently published a manuscript in which we studied the pitting and intergranular corrosion behaviour of Scalmalloy® of both as-built samples and subjected to final manufacturer-recommended heat treatment [25]. The results obtained in this work show that the as-built samples present a good general behaviour against pitting corrosion in 3.5 wt% NaCl solutions. From prolonged immersion studies for 15 days, it was concluded that small pits of 10–800 nm in diameter were formed, and Mg-Si and Al(Fe,Mn) phases were found to be related to pitting. Likewise, the heat treatment recommended by the manufacturer to achieve the best

* Corresponding author at: Departamento de Ciencia de los Materiales e Ingeniería Metalúrgica y Química Inorgánica, Universidad de Cádiz, Escuela Superior de Ingeniería, Puerto Real, Cádiz 11519, Spain.
E-mail address: leandro.gonzalez@uca.es (L. González-Rovira).

https://doi.org/10.1016/j.corsci.2023.111166
Received 21 December 2022; Received in revised form 14 March 2023; Accepted 4 April 2023
Available online 5 April 2023

mechanical properties and relieve stress, 325 ºC for 4 h, did not modify this good behaviour against the formation of pits. Moreover, the two types of samples are resistant to intergranular corrosion (IGC) according to ASTM G67 [26].

Another topic that has not been addressed so far in the literature is how the in-service behaviour of Scalmalloy® samples is affected after working at moderate temperatures for long periods of time. This information can help to define the framework of use of Scalmalloy®. It is known that traditional Al-Mg alloys with a weight percentage of Mg above 3.5%, such as 5083, can present problems of intergranular corrosion (IGC) and stress corrosion cracking (SCC) when subjected to heat treatments between 50 and 200 ºC [27–31]. This issue is related to the formation, in that temperature range, of the β-phase Al_3Mg_2, which precipitates preferably at the grain boundaries, although it can also form on particles rich in manganese [32–34]. The β-phase presents an anodic behaviour against the alloy matrix, being dissolved in certain corrosive media and thus causing the sensitisation of the material against IGC and SCC processes. According to [27], the degree of sensitisation (DoS) depends on both the temperature and the duration of the treatment, since both variables modify the amount of precipitated β-phase and the continuity of the network they form along the grain boundaries.

Li et al. [35] studied the susceptibility to IGC of the alloys Al-5.8Mg-0.4Mn, Al-5.8Mg-0.4Mn-0.1Sc-0.04Zr, and Al-5.8Mg-0.4Mn-0.25Sc-0.1Zr obtained by casting and sensitised with treatments at 130 ºC for 10, 72 and 168 h. These authors found that the addition of Sc and Zr improves the performance against the IGC and explained this improvement according to various experimental findings. Firstly, the Sc- and Zr-containing alloys have a higher relative proportion of low angle grain boundaries (LAGB) and lower of high angle grain boundaries (HAGB) than Al-5.8Mg-0.4Mn due to $Al_3(Sc_{1-x}Zr_x)$ dispersoids formed in the Sc- and Zr-containing alloys. Secondly, Al_6Mn particles are more likely to be rectangular or cubic shape when formed at HAGB, and rod-like when formed at LAGB. Thirdly, rectangular or cubic-shaped Al_6Mn can provide more heterogeneous nucleation sites for β-phase than rod-like shape. Therefore, β-phases find a lower number of nucleation sites in the Sc- and Zr-containing alloys because they have a lower relative proportion of HAGB and lower content of rectangular or cubic-shaped Al_6Mn. Consequently, β-phases are more likely to grow rather than nucleate at a new place in the Sc- and Zr-containing alloys, hindering the formation of a β-phase network along the grain boundaries. Similarly, Qiu et al. [36] added Sc and Zr to AA5182 (4.53%Mg, 0.22%Mn, 0.175%Fe in %wt.) by direct-chill casting and applied several heat treatments to different samples to modify their microstructure. Subsequently, they applied a sensitisation treatment at 175 ºC for 20 h. The studies performed unveiled an improvement in the resistance to IGC by adding Sc and Zr attributed to a high number density of nano-scaled coherent $Al_3(Sc_{1-x},Zr_x)$ dispersoids which resist recrystallization, and maintain a fine subgrain structure. They argue that the character of the subgrain structure is critical to prevent the occurrence of continuous intergranular Al_3Mg_2 precipitates during sensitisation.

Although the manufacturing conditions and microstructures are distinctly different, the IGC and SCC problems described in [27–31] for conventional Al-Mg alloys could be similarly produced in Scalmalloy® parts subjected to moderate temperatures, despite the increased corrosion resistance that the addition of Sc and Zr appears to provide. This possibility has not been studied to date in the literature. For this reason, in this paper, which is an extension of the work done in [25], the IGC and SCC susceptibility of Scalmalloy® samples subjected to sensitisation treatments at 150 ºC for up to three weeks is studied. This study is considered of high interest since the results obtained could determine the use of this alloy in industrial applications that involve exposure to temperatures between 50 and 200 ºC, even for short periods of time. The microstructures of the samples are characterized by SEM, STEM, X-ray analysis (EDS) and chemical attack with ammonium persulfate ($(NH_4)_2S_2O_8$). The effect of thermal sensitisation on the mechanical properties is studied by tensile and microhardness tests. Likewise, the effect of sensitisation on the corrosion behaviour is analysed by cyclic polarization, electrochemical impedance spectroscopy (EIS), nitric acid mass loss test (NAMLT) to measure the DoS to IGC, and by constant strain tests in 3.5 wt% NaCl solution alternate immersion to evaluate the susceptibility to SCC.

2. Material and methods

2.1. Material

The Scalmalloy® samples studied were manufactured by LPBF using an EOS M290 system using raw metallic powders supplied by Toyal and an energy density of 88 J/mm^3. A detailed description of the manufacturing process can be found elsewhere [19,25]. Table 1 shows the X-ray fluorescence (XRF) chemical analysis of the powder, expressed in wt% and performed with a BRUKER M4Tornado energy dispersive micro-XRF device.

The samples used as reference in this work, hereafter referred to as HT, were subjected to an air heat treatment at 325 ºC for 4 h as post-reatment, in order to optimise their mechanical properties. To study the possible sensitisation of the samples as a consequence of the operating temperature, HT samples were aged at 150 ºC for one, and three weeks in a Memmert UF30 furnace. Thus, three kinds of samples are studied: heat-treated (HT), heat-treated plus sensitisation at 150 ºC for one week (HT1W), and heat-treated plus sensitisation at 150 ºC for three weeks (HT3W).

The study was based on comparing the microstructure, mechanical properties, and behaviour against different forms of corrosion of HT and aged samples at 150 ºC for one and three weeks.

2.2. Characterisation

The microstructural characterisation was performed by scanning electron microscopy (SEM) in Hitachi SU1510 and FEI NOVA NanoSEM 450 microscopes, and energy-dispersive X-ray (EDX) analysis in transmission electron microscopy (TEM) using a FEI TALOS F200X devide. Electron-transparent samples for TEM were prepared in a FEI Scios2 DualBeam microscope. The percentages of area occupied by precipitates were measured using the software Fiji-ImageJ. In addition, the presence of β-phase particles in the samples was analysed by SEM after etching in 0.4 M $(NH_4)_2S_2O_8$ with additions of concentrated H_2SO_4 until pH = 1.2, as proposed in [27,28].

The mechanical properties were studied by means of tensile tests in a Shimadzu AG-X plus 100KN machine according to the ASTM E8/E8M [37] method B, and microhardness measurements in an Emcotest Duravision 20 durometer following the ASTM E384 [38] and applying 1 kgf. The strain of the specimens during the tensile tests was measured using an extensometer and the displacement of the crosshead. On one hand, the extensometer has higher precision but it is removed before fracture. This method covers the elastic zone and a portion of the plastic zone. On the other hand, the data from the crosshead are less accurate than those from the extensometer but they are recorded during the whole test. Young's modulus and yield strength are obtained employing the data acquired by the extensometer, due to its higher precision. While the tensile strength was measured using the data from the crosshead. The elongation and reduction of area were measured in each specimen after fracture. Further details about the mechanical tests can be found in [19]. In all cases the measurements were carried out in triplicate, presenting the average value obtained.

Table 1
Chemical composition of Scalmalloy® powder in wt% measured by micro-XRF.

Al	Mg	Sc	Zr	Mn	Fe	Ti	V
balance	4.702	0.871	0.378	0.690	0.170	0.001	0.048

2.3. Corrosion tests

The electrochemical characterisation was accomplished by recording the open circuit potential (OCP) for one hour before the acquisition of cyclic polarisation curves and electrochemical impedance spectra. The samples tested were previously grinded with SiC paper at 1200 grit and the area exposed was 1.0 cm^2. Three specimens were measured per condition. In all cases, 3.5 wt% NaCl aqueous solutions maintained at 25 °C, an Avesta cell with a three-electrode configuration, a PGSTAT204 Metrohm potentiostat, and Nova 2.1.4 software were used. A standard calomel electrode (SCE, 0.244 V/SHE, 25 °C) and graphite rods were employed as reference and counter electrode, respectively. The cyclic polarisation curves were obtained with + 0.167 mV/s voltage scanning velocity from − 0.01 V_{OCP} until a current of 5×10^{-4} A was reached, when the voltage sweep was reversed. The range of frequency for the EIS tests was from 1 kHz to 0.01 Hz, with a perturbation of ± 10 mV_{RMS} sinus amplitude around OCP. Five impedance values were registered per each frequency decade. Nova 2.1.4 software was used to fit the EIS spectra.

The intergranular corrosion behaviour has been studied by performing nitric acid mass loss tests (NAMLT) according to ASTM G67–04 following the procedure described in [25].

Finally, stress corrosion tests were performed according to ASTM G47–98 for aluminium alloys [39]. To carry out the test, blocks of material were manufactured and heat treated to obtain HT, HT1W and HT3W samples. These blocks were subsequently machined to obtain standardised specimens according to the applicable standard. The tests were performed using SCC calibrated proof rings from CORMET testing systems, with capacity range from 10 to 25 kN, equipped with microswitches capable to detect the moment where the samples break. The equipment can be seen in Fig. 1. While the samples were loaded, they were inside a glass cylinder and subjected to cycles comprising 10 min of immersion in 3.5 wt% NaCl and 50 min in air. The system to apply these cycles by introducing and removing the corrosive solution in and out of the glass cylinders has been designed in our laboratories. The concentration of the NaCl solution was monitored during the tests by means of conductivity measurements and corrected accordingly when required. The tests finished when the samples fail or they reach 20 days without failure.

3. Results

3.1. Microstructure

Fig. 2 depicts the 3D microstructure of a cube extracted from an HT sample observed by BSE-SEM. The superposition of semispherical melt pools formed by equiaxed fine-grained zones (FGZ) at the shell and elongated coarse-grained zones (CGZ) in the core is observed. The cross-section of the melt pools can be distinguished in YZ- and XZ-planes, which are equivalent. Hence, columnar grains are observed in CGZ and equiaxed grains in the FGZ. Meanwhile, the microstructure in XY-planes is the transversal view of the microstructure described on the YZ- and XZ-planes. There are two groups of round grains featuring different diameters. The small grains are placed in the boundaries of the melt pools and correspond to FGZ and the coarse grains correspond to transverse sections of elongated grains in the CGZ inside the melt pools. This bimodal microstructure is characteristic of metallic samples manufactured using LPBF technology and has already been described for Scalmalloy® [25]. A more detailed description of the microstructure can be found elsewhere [19,25].

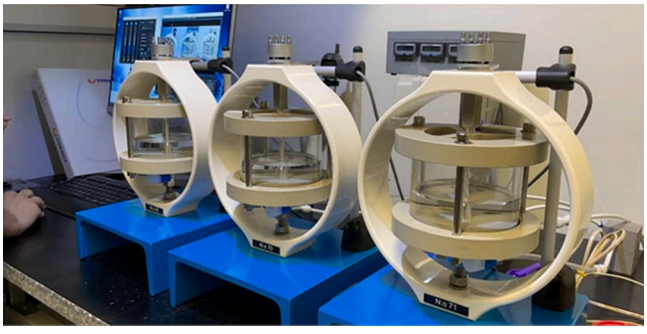

Fig. 1. Stress Corrosion Cracking equipment.

Fig. 3 includes BSE-SEM images at different magnifications of the three different samples studied. Thus, the images in Fig. 3(a-c) correspond to the HT sample. The images in Fig. 3(d-f) correspond to the HT1W sample obtained by treating the HT sample in an oven at 150 °C for one week. Finally, the images in Fig. 3(g-i) correspond to the HT3W sample, obtained by prolonging the oven treatment at 150 °C for three weeks. Fig. 3(a-c) show that the microstructure of the melt pools in the HT sample has the two separate zones described above: FGZ in the shells and CGZ in the cores.

Comparing the image in Fig. 3(a) with those included in Fig. 3(d) and (g), no significant changes are observed between the three types of samples. Thus, it has been determined, after measuring around 150 grains in each sample, that in the FGZ the average grain size is 0.7 ± 0.3 μm for the HT sample, and 0.6 ± 0.2 μm and 0.7 ± 0.2 μm for the HT1W and HT3W samples, respectively. In the CGZ the average grain size in its longest dimension for sample HT is 6.7 ± 5.7 μm, and 6.4 ± 3.9 μm and 8.6 ± 7.2 μm for samples HT1W and HT3W. Fig. 4 shows the analysis of the shape factor obtained for the CGZ grains for the HT, HT1W and HT3W samples. It can be seen that the clearly predominant shape factors are 2, 3 and 4. That is, a typical grain in CGZ in all three sample types is roughly three times longer along the manufacturing direction than in the perpendicular direction. Therefore, it can be concluded that a heat treatment in an oven at 150 °C, with a duration between one and three weeks, does not generate significant changes in the morphology of grains, neither those present in FGZ nor in CGZ. This behaviour is consistent with the high resistance to recrystallization at temperatures below 400 °C shown by this alloy, attributed to the presence of fine $Al_3(Sc_{1-x},Zr_x)$ precipitates highly dispersed at the grain boundaries [12,40].

Fig. 3(b), (e) and (h) show the BSE-SEM images acquired at higher magnification in FGZ of each of the three samples studied. They reveal that the treatment at 150 °C, Fig. 3(e) and (h), lead to an increase in the number of dark precipitates compared to the HT sample, Fig. 3(b). These precipitates tend to accumulate mainly at intergranular positions, whereas they are not present at intragranular positions in FGZ. Images in Fig. 3(c), (f) and (i) were acquired at higher magnification in the CGZ of HT, HT1W and HT3W samples, respectively. The same effect described for FGZ is observed, i.e., the heat treatment at 150 °C for up to three weeks causes the formation of dark intergranular precipitates in CGZ. Likewise, there are no dark precipitates at intragranular positions in CGZ of samples HT1W or HT3W. In addition, the presence of white precipitates can be observed in the images corresponding to the sample without ageing, HT, Fig. 3(a-c), whose distribution seems to be not significantly modified in the samples treated at 150 °C, Fig. 3(d-f) and Fig. 3(g-i). Estimates of the percentages of the area occupied by the dark and white precipitates were measured using the software Fiji-ImageJ in 5 images per type of sample, containing these images FGZ and CGZ. The dark precipitates account for 0.06 ± 0.02%, 1.87 ± 0.51% and 1.26 ± 0.32% of the total area in HT, HT1W and HT3W, respectively. Therefore, an increase in the percentage of dark particles is observed when the samples are sensitized at 150 °C for 1 week, and there is no significant change when the treatment is prolonged from 1 to 3 weeks. While the areas populated by the white precipitates are 0.48 ± 0.22% for HT, 0.26 ± 0.07% for HT1W and 0.23 ± 0.09% for HT3W. Thus, according to this characterisation, the content of white precipitates is not substantially altered by the treatment at 150 °C.

It should be noted that, since these images were obtained with the

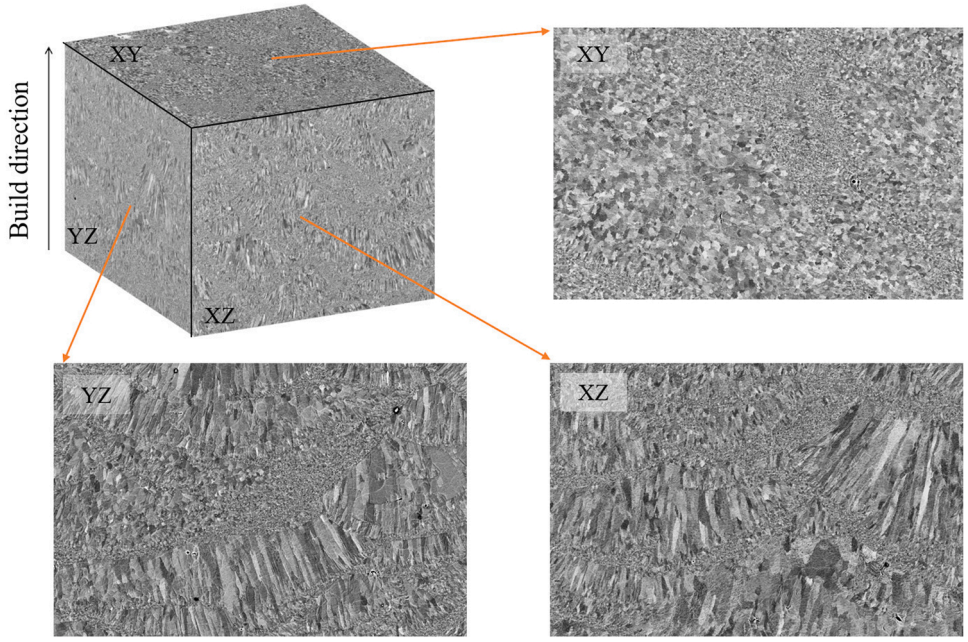

Fig. 2. Schematic 3D representation of the microstructure of HT sample.

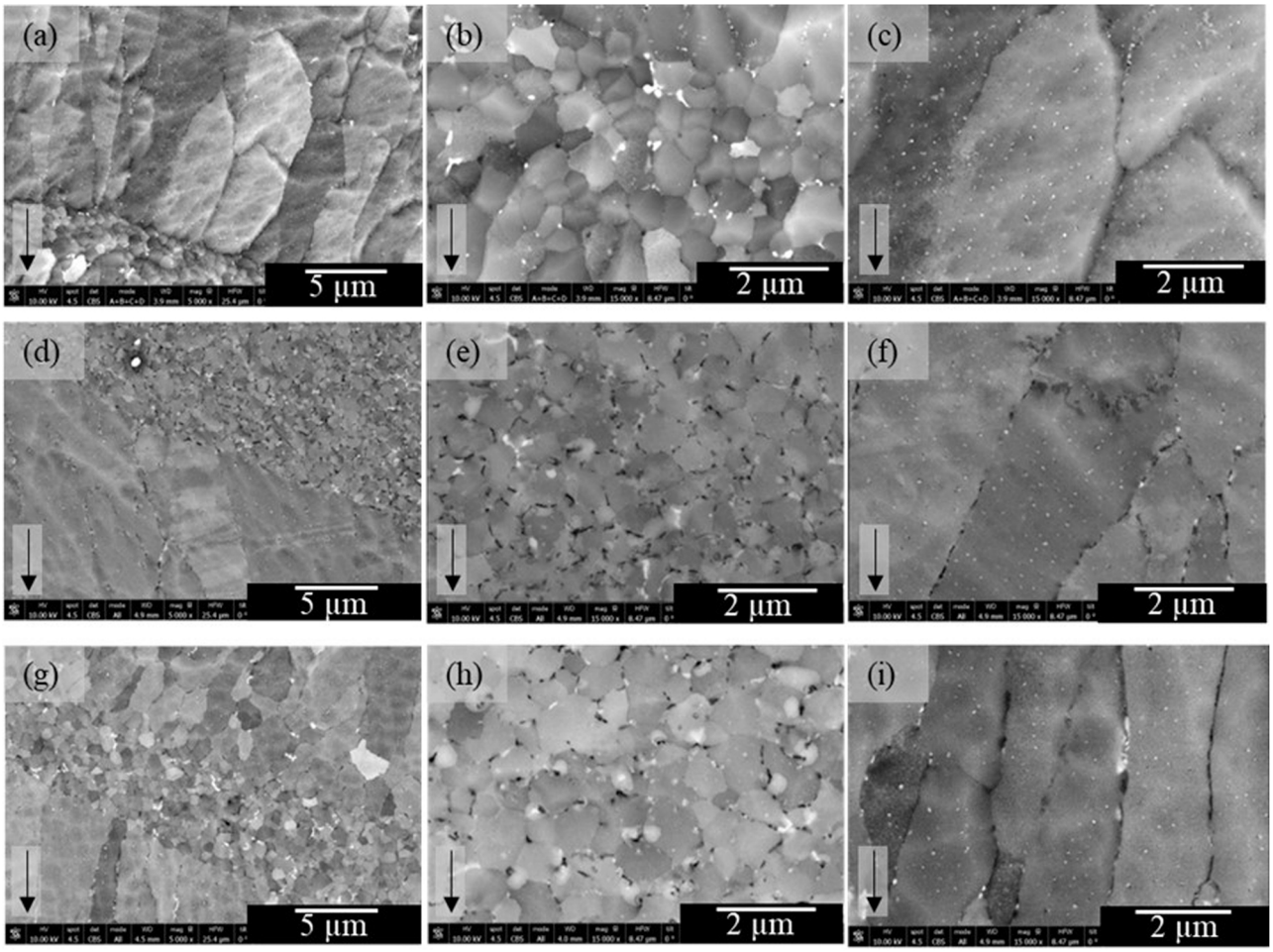

Fig. 3. BSE-SEM images showing the microstructure for a XZ-plane of HT sample ((a)-(c)), HT1W sample ((d)-(f)) and HT3W sample ((g)-(i)). Building direction indicated by arrows.

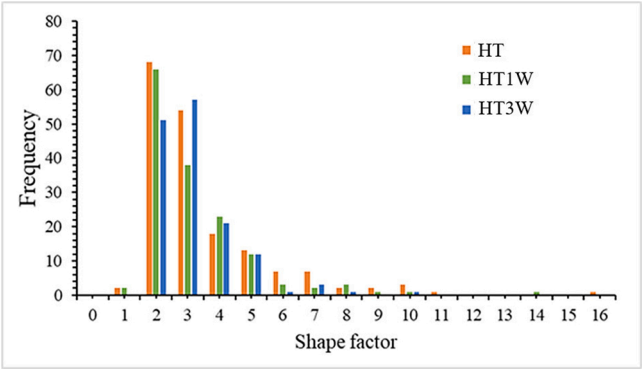

Fig. 4. Shape factor distribution of grains in CGZ.

backscattered electron detector, the dark and white shade of the precipitates in comparison with the matrix would indicate that the precipitates contain elements with lower and higher atomic numbers than aluminium (Z = 13), respectively. A detailed study of the composition of the precipitates is described below.

With the objective of analyse the chemical composition of the precipitates identified in Fig. 3, elemental distribution maps were acquired by EDS-TEM. For this purpose, lamellae were extracted using FIB microscopy from FGZ and CGZ. The elemental distribution maps for Al, Mg, Sc, Zr, Si, Fe, Mn, and O are included in Fig. 5 and Fig. 6. Thus, the maps included in Fig. 5 were acquired in FGZ of the three samples, while those in Fig. 6 were acquired in CGZ. Images obtained by high angle annular dark field scanning transmission spectroscopy (HAADF-STEM) of the three zones analysed are also included in both figures.

Previous characterisation work of the HT condition carried out in our research group [25] identified different types of precipitates: i) Mg-rich phases, ii) Mg-Si phases, iii) Al(Sc,Zr) phases, iv) Al(Fe,Mn) phases, and v) different oxygen-rich particles attributed to various oxides. The presence of these types of phases in Scalmalloy® samples has also been described by other authors [7,40,41].

The changes that occur in the distribution of precipitates as a consequence of the sensitisation heat treatment are detected when contrasting the elemental distribution maps of the HT, HT1W and HT3W samples. Thus, when comparing the Mg maps, the main effect observed is the formation of Mg-rich precipitates at the grain boundaries after the treatment at 150 ºC. This effect is observed both in the FGZ, Fig. 5, and in the CGZ, Fig. 6. The sizes of these precipitates are variable, but most of them are in the range of 20–60 nm in width and 50–400 nm in length. Moreover, Mg-rich precipitates do not suffer substantial modifications when the ageing treatment is extended from one week up for three weeks. Besides, Sc maps show that the 150 °C treatment leads to the formation and/or coarsening of Sc-rich precipitates in the FGZ, Fig. 5, while new Sc-rich precipitates are not clearly perceived in the CGZ after the thermal aging, Fig. 6. While Sc-rich particles in the HT sample exhibit sizes below 20–30 nm approximately, particles with several tens of nm can easily be found in the HT1W and HT3W. Sc-rich particles can be reasonably attributed to $Al_3(Sc_{1-x},Zr_x)$ precipitates, characteristic of Al-Sc-Zr alloys [16,42–44].

Additionally, different types of precipitates that are not affected by the heat treatment can be found in Fig. 5 and Fig. 6. Among them, there are Mg- and Si-rich phases located at the grain boundaries in the FGZ, Fig. 5, and in intragranular zones in the CGZ, Fig. 6. Fe-rich precipitates are also observed at the grain limits in the FGZ and at intragranular positions in the CGZ. A third group comprises Fe- and Mn-rich precipitates. Finally, the presence of Fe-, Mg-, Si- and O-containing particles should be noted, which also show no signs of change when the samples are treated at 150 ºC.

To emphasise the presence of Mg in the intergranular precipitates formed by treating the samples at 150 °C, linear EDX profiles of Mg and Al concentration were recorded in the transverse direction of some of these precipitates. Fig. 7 includes one of these profiles. It can be clearly observed how the intensity of the Mg signal increases as it crosses the intermetallic, while the Al signal decreases slightly as a consequence of the Al content in the precipitate being lower than the Al content in the matrix.

Numerous studies of wrought alloys have revealed that the β-phase, Al_3Mg_2, is formed by heterogeneous precipitation at grain boundaries and on manganese-rich phases because the activation energy for heterogeneous nucleation is lower than that for homogeneous nucleation in the matrix [33,45]. It is also generally accepted that the nucleation process and growth of the β-phase is controlled by pipe diffusion via dislocations [36,45–47].

In [25,48,49], it is proposed that it is possible to reveal the presence of β-phase particles, Al_3Mg_2, in wrought Al-Mg alloys by selective etching of this phase with an ammonium persulphate solution. Using this procedure, HT, HT1W and HT3W samples were attacked in order to determine the distribution of the β-phase over larger areas than those studied by STEM-EDX. Fig. 8 contains BSE-SEM images showing XZ planes of the three samples studied after being attacked for 40 min with 0.4 M $(NH_4)_2S_2O_8$ solution at pH 1.2. Thus, in Fig. 8(a) and (b), corresponding to the HT sample, the occurrence of isolated β-phase particles is revealed by corresponding isolated holes, especially in FGZ. In the images of the HT1W sample, Fig. 8(c) and (d), there is an increase in the concentration of β-phase particles compared to the HT sample, which seem to accumulate at the grain boundaries. Finally, in the images belonging to the HT3W sample, Fig. 8(e) and (f), a slight increase in the degree of attack is observed with respect to the HT1W sample, so that the HT3W sample is clearly characterised by numerous continuous lines along the grain boundaries produced by the dissolution of β-phase particles, both in FGZ and CGZ. According to [27], the formation of continuous lines of β-phase particles and their extent determines the intergranular corrosion performance of conventional Al-Mg alloys.

The level of continuity observed in the network of β-phase particles in the samples studied in this work appears to be lower than that described by other authors for samples of alloy 5083, with a similar Mg content to Scalmalloy®, and thermally aged under similar conditions. Thus, Searles et al. [31] determined by TEM the formation of a continuous β-phase film on samples treated at 150 ºC for 189 h. On the other hand, Ress et al. [27] found the complete dissolution of grain boundaries when 5083 samples treated at 150 °C for more than 7 days were attacked with ammonium persulphate. In [27], it is reported that grain boundaries become β-phase saturated after around 7 days of ageing. For this reason, samples treated for periods from 7 of up to 30 days are characterised by intragranular β-phase particles.

Therefore, the results shown in Fig. 8 indicate that Scalmalloy® exhibits a higher resistance than 5083 aluminium alloy to form a continuous β-phase network when heat treated at temperatures close to 150 °C.

3.2. *Mechanical properties*

The mechanical properties of the three types of samples prepared were evaluated by tensile tests according to ASTM E8/E8M [37]. The comparison of the results obtained allows determining the effect of the treatment at 150 ºC on these properties. Fig. 9 displays the stress-strain response of the samples tested. Fig. 9(a) uses the strain data obtained with the crosshead and Fig. 9(b) the acquired with the extensometer. The tests were carried out in triplicate. All samples show a typical ductile behaviour with a near horizontal section of the stress-strain curve after the yield strength is surpassed and fracture strain higher than 9%. The fluctuations of the signals observed in the plastic zone of the curves in Fig. 9(a) are generated by the data logging software automatically when the test is paused to remove the extensometer. These fluctuations do not affect the precision of the results. Table 2 includes Young's modulus (E) and yield strength (RP) calculated from

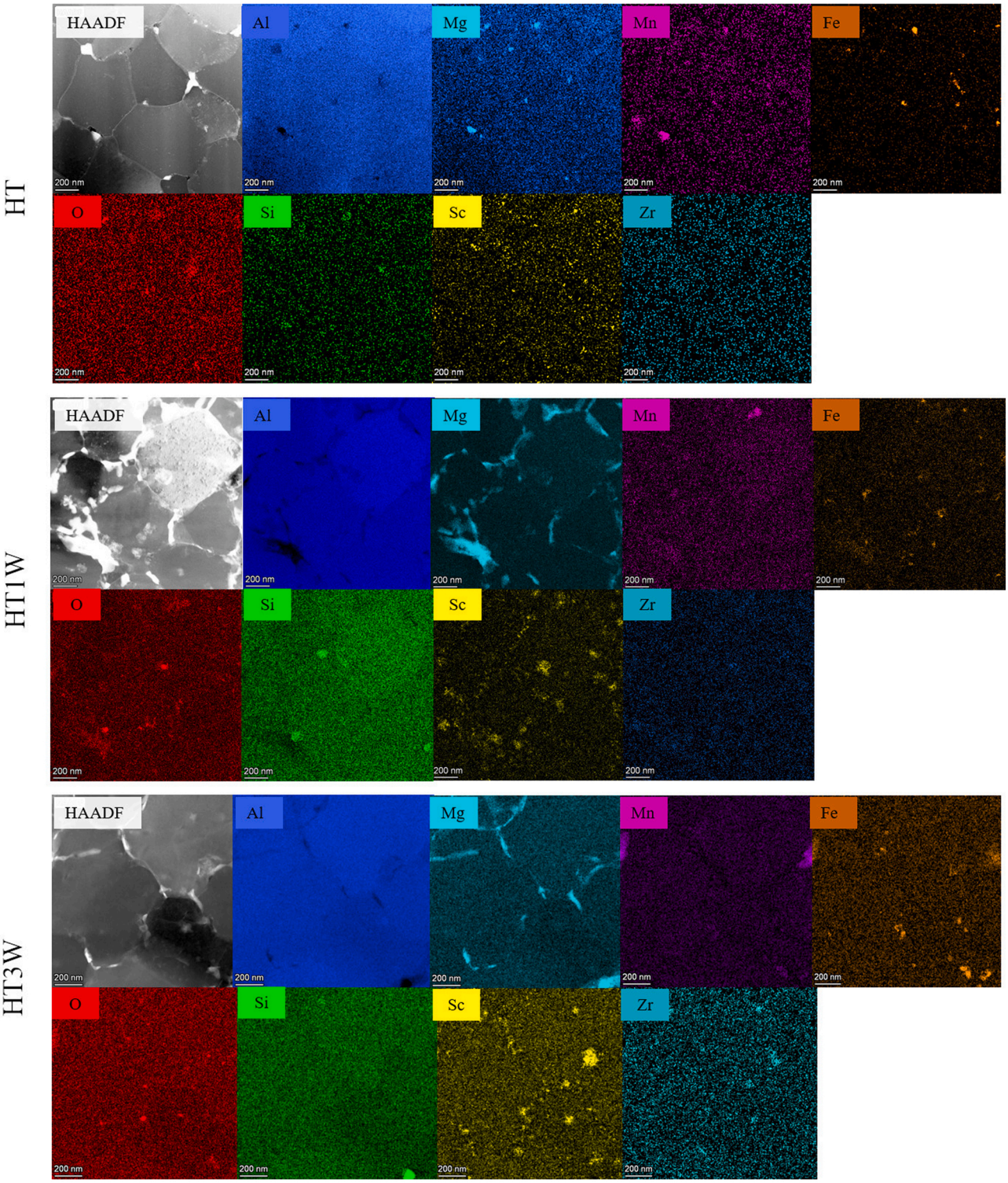

Fig. 5. HAADF-STEM images of FGZ of HT, HT1W and HT3W samples. EDX mapping for Al, Mg, Mn, Fe, O, Si. Sc, and Zr.

curves in Fig. 9(b), tensile strength (RT) from Fig. 9(a), and percentage of elongation and percentage of the reduction of area measured in each specimen after fracture. In this table, Vickers hardness data obtained using ASTM E384 standard [38] are included as well.

On one hand, Young modulus, elongation, reduction of area and hardness do not suffer significant changes after the thermal treatment. On the other hand, yield strength and tensile strength exhibit small differences. RP values are 454 ± 3 MPa, 468 ± 3 MPa and 459 ± 3 MPa for the HT, HT1W and HT3W samples, respectively. While the RT values move from 509 ± 6 MPa for the HT sample, up to 527 ± 2 MPa and 528 ± 1 MPa for the HT+ 1 W and HT+ 3 W samples, respectively. The slight variations of RP and RT of around 1–3% could be due to a minor inter-sample variability and/or a slight increase in hardening by precipitation of new $Al_3(Sc_{1-x},Zr_x)$ phases. Although the latter possibility is not reflected in the hardness results, which are 165 ± 3 HV, 162 ± 4 HV and 166 ± 4 HV for the HT, HT1W and HT3W samples. Moreover, only coherent $Al_3(Sc_{1-x},Zr_x)$ phases improve the hardness and coherency loss is reported to take place at sizes higher than ≃ 21.5 nm [12]. Many of

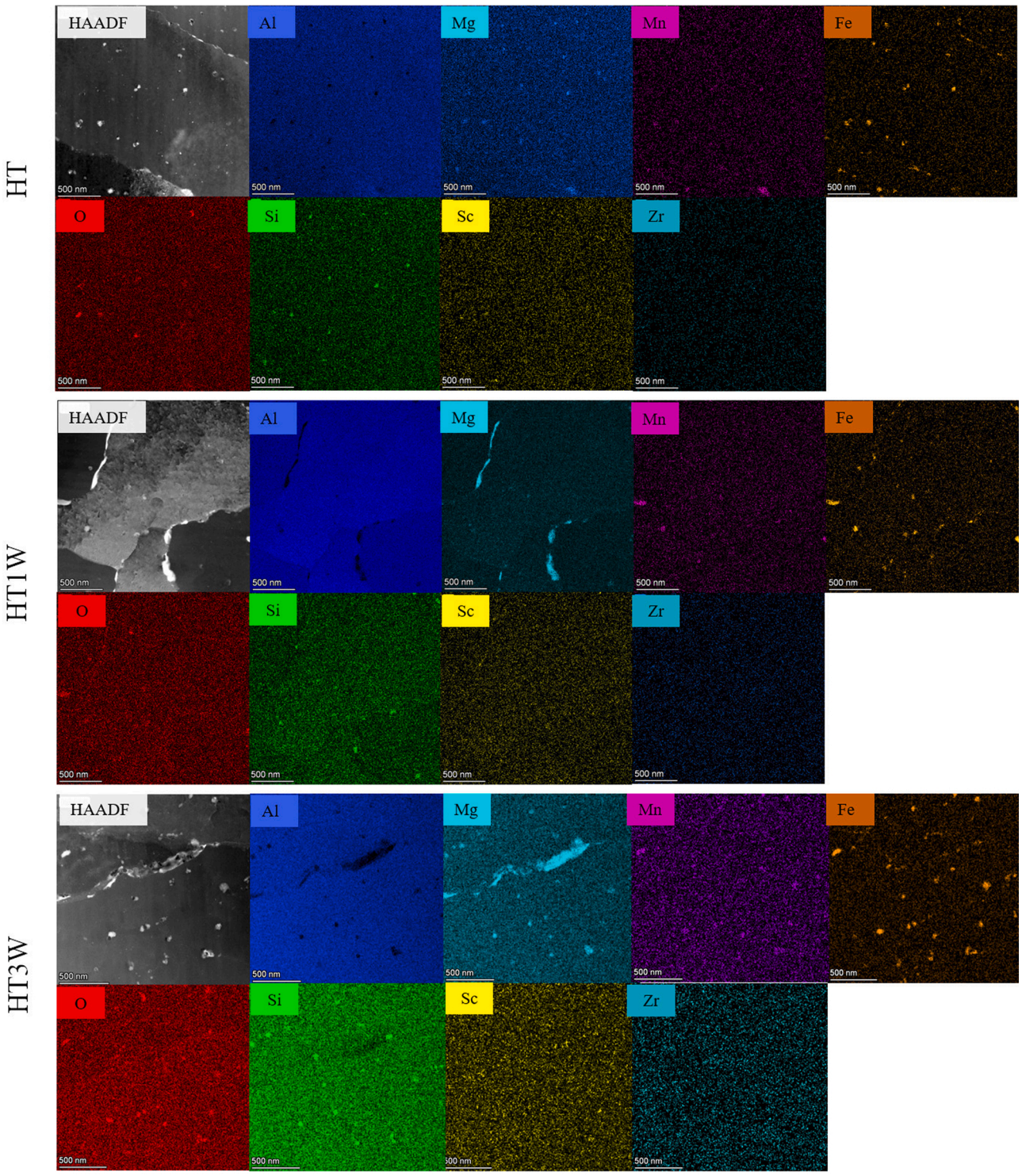

Fig. 6. HAADF-STEM images of CGZ of HT, HT1W and HT3W samples. EDX mapping for Al, Mg, Mn, Fe, O, Si. Sc, and Zr.

the Sc-rich particles in Fig. 5 are coarser than 21.5 nm and, therefore, they do not give rise to precipitation hardening. In any case, the variations in mechanical properties are, if any, very small. Gao and Quesnel [30] also found no variations in the mechanical properties of the AA5083 after treatments at 175 °C for different times up to 360 h. Similarly, Searles et al. [31] report no variations of mechanical properties of AA5083 sensitised at 150 °C up to 333 h. Therefore, based on the microstructure study carried out in this research together with the results obtained by other authors on Al-Mg alloys, it can be concluded that neither the formation of β-phase nor the reduction of Mg concentration in the matrix caused by this precipitation affect the mechanical properties of Scalmalloy® significantly.

Fig. 10 shows various SE-SEM images of the fracture surface of the three types of samples studied. Fig. 10 (a), (d) and (g) show a reduction in the diameter of the specimen in the fracture zone, characteristic of ductile behaviour and in line with the stress-strain curves represented in Fig. 9 and the values in Table 2. At higher magnification, Fig. 10 (b), (e) and (h), the presence of dimples characteristic of ductile fracture of the material can be seen in all the samples. However, there are also small areas of cleavage showing brittle separation between grains. Some of

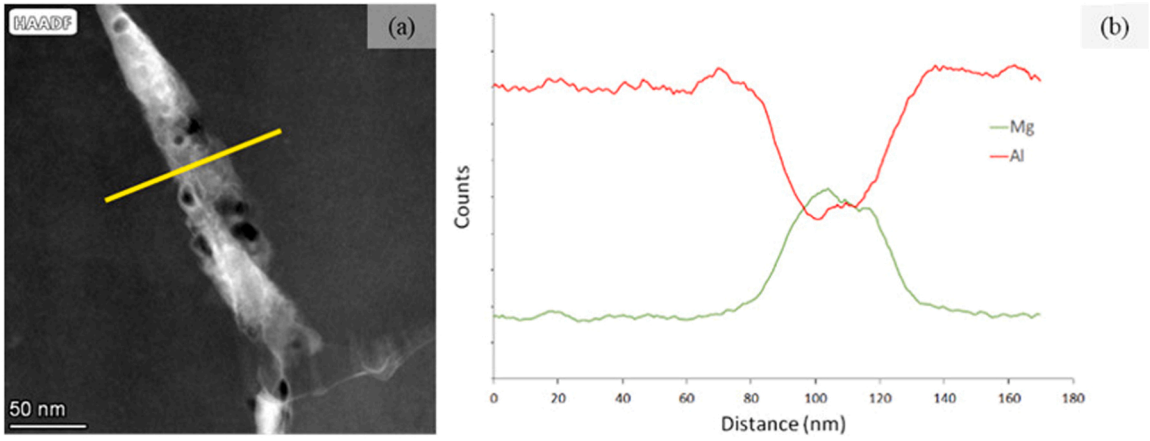

Fig. 7. (a) HAADF-STEM image of a grain boundary in HT3W sample. (b) EDS profile of Mg and Al signals along the yellow line marked in (a).

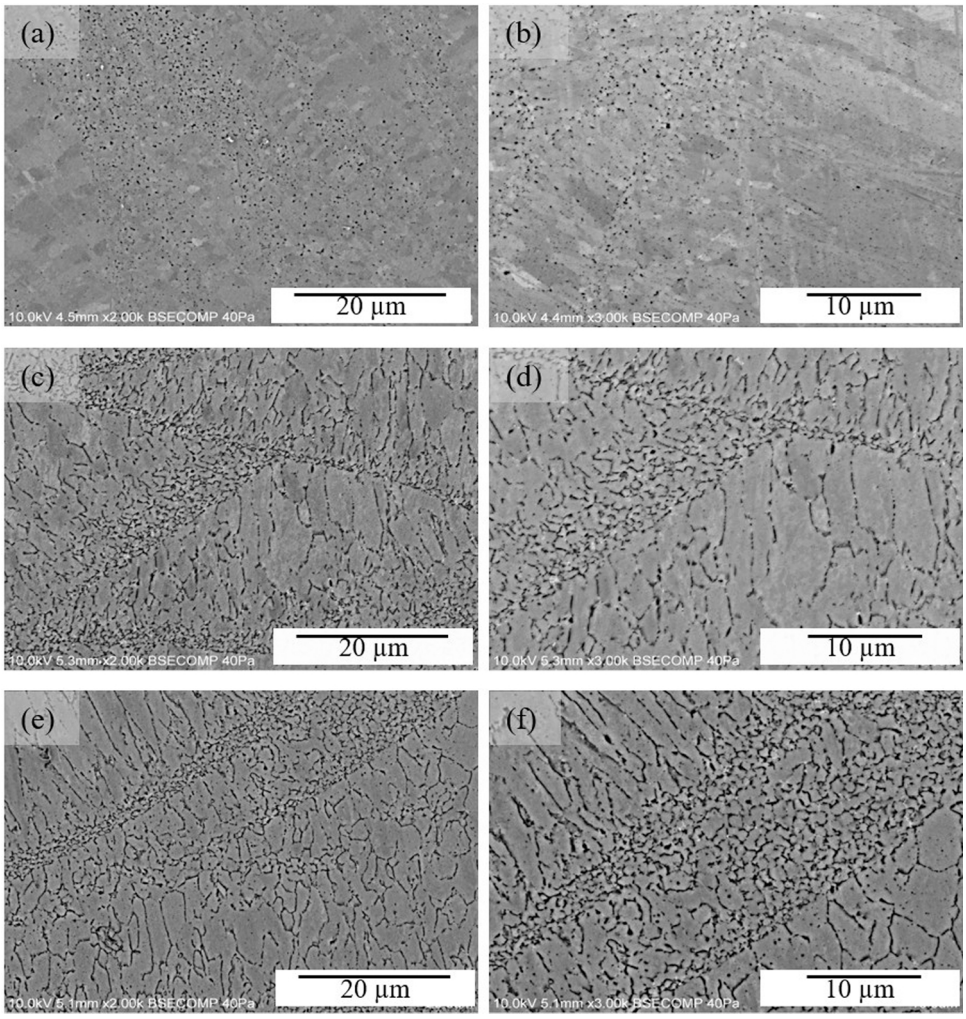

Fig. 8. BSE-SEM images of the samples after etching in $(NH_4)_2S_2O_8$ solution. (a-b) HT sample. (c-d) HT1W sample. (e-f) HT3W sample.

these latter zones are indicated by arrows in Fig. 10 (c), (f) and (i). Hence, the results included in Fig. 10 state that the ageing at 150 °C does not produce changes in the fracture mode of Scalmalloy® samples assessed by tensile tests.

3.3. Cyclic polarization

Fig. 11 shows one representative OCP record and one polarization curve per condition. The average values of the electrochemical parameters along with their corresponding standard deviations obtained from all the polarisation curves are summarised in Table 3.

The OCP curves recorded during 1 h have the same behaviour for the

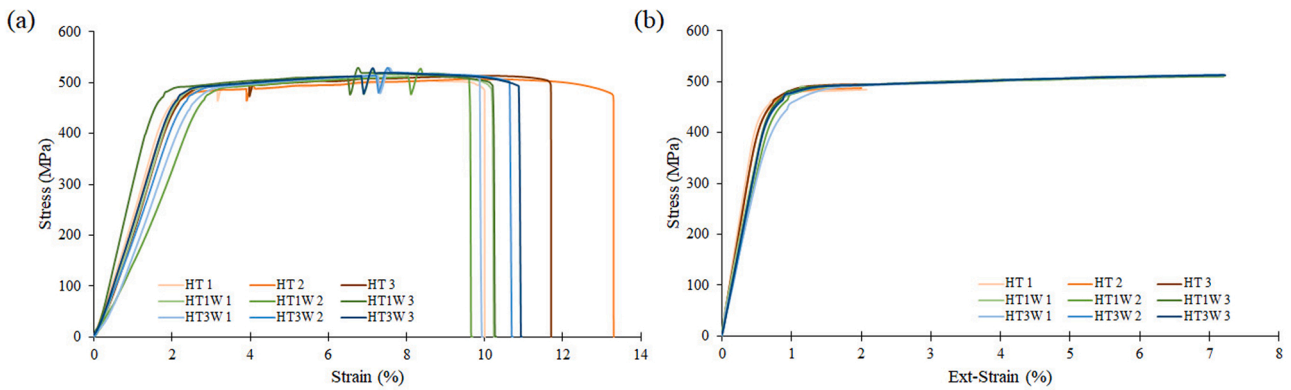

Fig. 9. Stress-strain curves for samples: HT (orange), HT1W (green) and HT3W (blue). a) Strain measured with the crosshead, b) strain measured with the extensometer.

Table 2
Mechanical properties measured for samples HT, HT1W and HT3W.

	Young Modulus, E (GPa)	Yield Strength, RP (MPa)	Tensile Strength, RT (MPa)	Elongation (%)	Reduction of area (%)	Hardness (HV)
HT	64 ± 3	454 ± 3	509 ± 6	11 ± 2	16 ± 6	165 ± 3
HT1W	67 ± 4	468 ± 3	527 ± 2	12 ± 2	18 ± 3	162 ± 4
HT3W	67 ± 3	459 ± 3	528 ± 1	12 ± 1	17 ± 3	166 ± 4

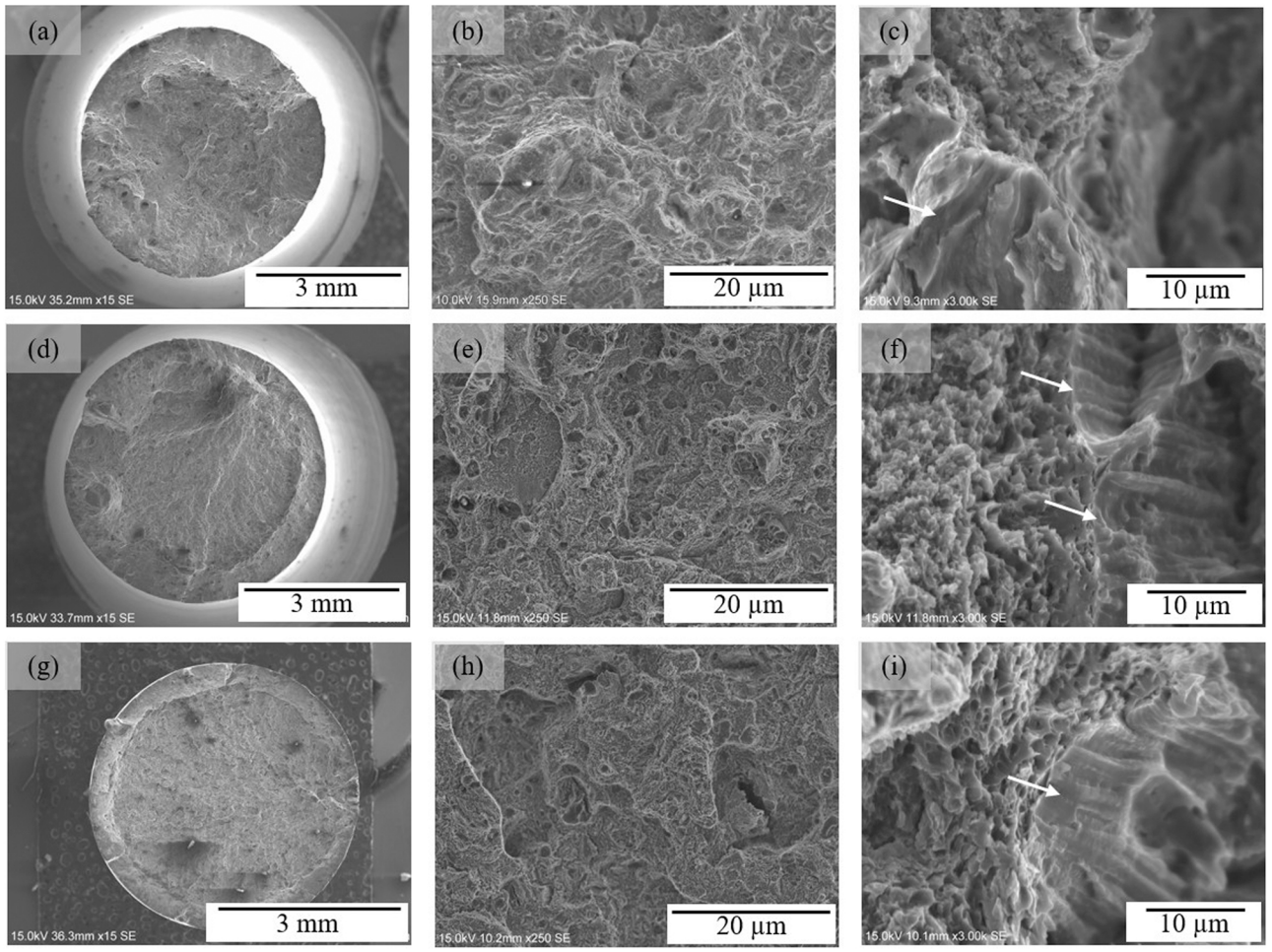

Fig. 10. SE-SEM-fractography of samples HT (a-c), HT1W (d-e), and HT3W (g-i).

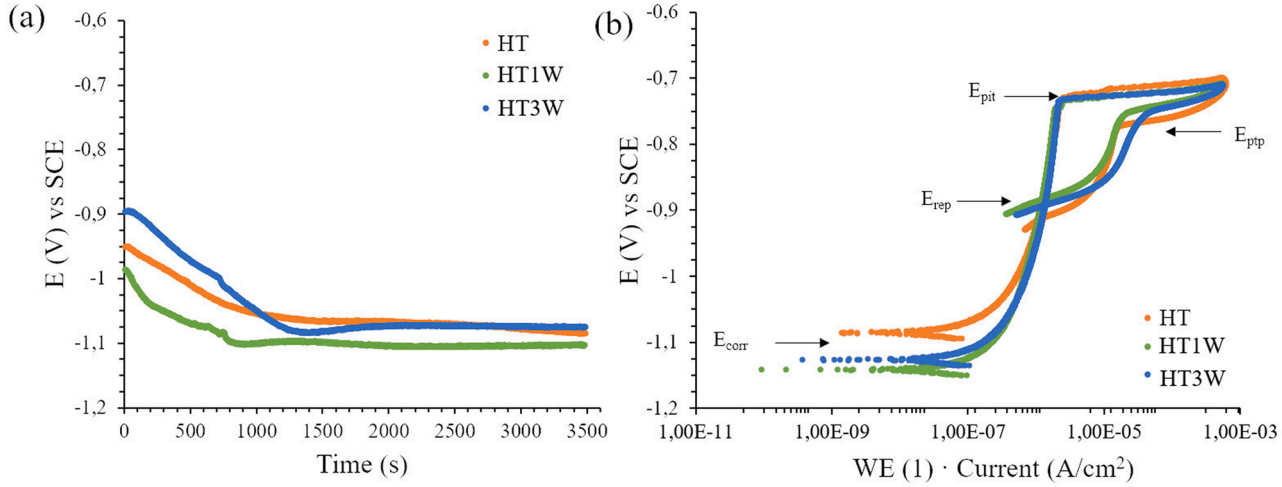

Fig. 11. Representative (a) OCP recorded during 60 min and (b) cyclic polarization curves.

Table 3
Electrochemical data from cyclic polarisation curves. Errors in brackets expressed as standard deviation.

	E_{corr} (mV_{SCE})	I_{pas} ($\mu A/cm^2$)	E_{pit} (mV_{SCE})	E_{ptp} (mV_{SCE})	I_{rep} ($\mu A/cm^2$)	E_{rep} (mV_{SCE})	$\lvert E_{pit} - E_{ptp}\rvert$ (mV_{SCE})	$\lvert E_{ptp} - E_{rep}\rvert$ (mV_{SCE})	$\lvert E_{pit} - E_{rep}\rvert$ (mV_{SCE})	$\lvert I_{rep} - I_{pas}\rvert$ ($\mu A/cm^2$)
HT	-1081	1.60	-733	-776	12.14	-915	43	139	182	10.54
	(± 10)	(± 0.19)	(± 1)	(± 2)	(± 2.84)	(± 2)	(± 3)	(± 4)	(± 3)	(± 3.03)
HT1W	-1108	1.64	-742	-757	12.55	-888	15	131	146 (± 10)	10.91
	(± 49)	(± 0.26)	(± 7)	(± 2)	(± 2.91)	(± 3)	(± 9)	(± 5)		(± 3.17)
HT3W	-1057	1.62	-741	-758	17.32	-897	21	139 (± 10)	156 (± 10)	15.62
	(± 62)	(± 0.13)	(± 2)	(± 2)	(± 0.47)	(± 8)	(± 4)			(± 0.60)

three types of samples, Fig. 11 (a). The potential takes initial values in the range between − 0.9 V_{SCE} and − 1.0 V_{SCE} and then decreases until reaching a stable OCP value of, approximately, − 1.1 V_{SCE}. This drop in potential is related to a slight degradation of the passive layer of the alloy, as discussed in previous investigations [25]. It should be highlighted the absence of transits that could be associated with pitting corrosion processes in all the samples analysed.

Regarding the polarization curves, Fig. 11 (b), all three conditions show curves with a passivity zone in the forward scan. The corrosion potentials (E_{corr}) and current density in the passivity zone (I_{pas}) are similar in the three samples, with values in the vicinity of − 1100 mV_{SCE} and 1.61 $\mu A{\cdot}cm^{-2}$, respectively. The pitting potential (E_{pit}) values are very similar, − 733 ± 1 mV_{SCE} for the HT sample, − 742 ± 7 mV_{SCE} for the HT1W sample, and − 741 ± 2 mV_{SCE} for the HT3W sample.

In our previous work [25], the pitting corrosion behaviour of HT-type samples in 3.5 wt% NaCl solution was studied. The analyses of the immersion tests reported in that work attributed the pitting that appears in the vicinity of E_{corr} to galvanic corrosion caused by Mg-Si and Al(Fe,Mn) precipitates. Here, in the results included in Section 3.1 of the current work, the samples treated at 150 °C show the formation of $Al_3(Sc_{1-x},Zr_x)$ precipitates and also intergranular β-phase precipitates (Al_3Mg_2). On one hand, according to the literature, the $Al_3(Sc_{1-x},Zr_x)$ phases have only a weak cathodic behaviour against Aluminium and feature poor behaviour to sustain the reduction of oxygen [50,51]. Consequently, the formation of new $Al_3(Sc_{1-x},Zr_x)$ phases shown in the STEM-EDS study would have little influence on E_{corr} and E_{pit}, as reported by other authors [25,50,52,53]. On the other hand, with respect to the β-phase, Searles et al. [31] report an E_{corr} around − 1300 mV_{SCE} for this phase and a passivity zone until $E_{pit} = -920$ mV_{SCE} in 3.5 wt% NaCl solution. Similar figures are reported by Lyndon et al. [54] for the β-phase in 0.01 M NaCl solution at pH 6 and 8, with $E_{corr} = -1313 \pm 59$ mV_{SCE} at pH 6, $E_{corr} = -1310 \pm 50$ mV_{SCE} at pH 8, and $E_{pit} \approx -900$ mVSCE in both pH cases. While Birbilis and Buchheit [55] obtained slightly different values, with $E_{corr} = -1162$ mV_{SCE} and $E_{pit} = -969$ mV_{SCE} in 0.6 M NaCl (≈ 3.5 wt% NaCl).

According to Table 3, Scalmalloy® present $E_{corr} \approx -1100$ mV_{SCE} in 3.5% NaCl. If any of the E_{corr} values proposed in the literature for the β-phase are taken into account, it is concluded that this phase would have an anodic behaviour towards the Scalmalloy® matrix at − 1100 mV_{SCE}. For this reason, the β-phase particles present in the samples should dissolve in a similar way to other Mg-rich phases [55–57]. However, the passive state of the β-phase at − 1100 mV_{SCE} makes its dissolution severely hampered, if not prevented, during the recording of the OCP curves shown in Fig. 11(a). This would explain why the OCP records of the three samples studied are similar so that the presence of β-phases in the samples treated at 150 °C does not show up in these curves.

As previously mentioned, the values of E_{pit} in Fig. 11 (b) and Table 3 are quite similar. In principle, the appearance of the β-phase in the microstructure of the aged samples would produce a shift of E_{pit} from − 733 ± 1 mV_{SCE} in the HT sample to values closer to the E_{pit} of the β-phase, around ≈ −950 mV_{SCE}, in the aged samples. However, experimentally, the magnitude of this shift is found to be very small, $E_{pit} = -742 \pm 7$ mV_{SCE} for the HT1W sample, and − 741 ± 2 mV_{SCE} for HT3W. Jain et al. [58] found similar negligible shifts for the E_{pit} of unsensitised AA5083 and sensitised for various times at 100 °C, which decreases from around – 0.64 mV_{SCE} down to – 0.65 mV_{SCE} when the material was sensitised for 14 days, and to – 0.66 mV_{SCE} when sensitised for 30 days. Jain et al. also reported a displacement of the anodic branches to higher current densities of around 1 or 2 orders of magnitude upon sensitisation time increased. This last phenomenon is not suffered by Scalmalloy® in Fig. 11 (b).

Continuing with the description of the polarisation plots in Fig. 11 (b), according to [59], the diminution in current density at the beginning of the reverse curve corresponds to the beginning of the passivation of the pits previously formed. Then, the curves have an inflection point where the pitting transition potential (E_{ptp}) is defined. At this point, all the pits of a first group, which we will name group A, have been

passivated [25]. At potentials below E_{ptp}, the decrease in current density corresponds to the repassivation process that continues, in this case only with a second type of pits that are more difficult to repassivate and that we will name group B. The current density continues to decrease until the repassivation potential (E_{rep}) is reached, when all the pits in group B attain passivity because of $E_{rep} > E_{corr}$. Based on the literature [25,27], the distance between E_{pit} and E_{ptp}, and between E_{pit} and E_{rep}, are related to the difficulty of repassivating pits in groups A and B, respectively. Hence, the largest $|E_{pit} - E_{ptp}|$ and $|E_{pit} - E_{rep}|$, the more difficult it is to repassivate each associated group of pits.

As can be seen in Table 3, $|E_{pit} - E_{ptp}|$ slightly decreases when the alloy undergoes the ageing step from a value of 43 ± 3 mV_{SCE} for the HT sample down to 15 ± 9 mV_{SCE} for the HT1W, and 21 ± 7 mV_{SCE} for HT3W. Although this reduction should be taken with caution because the difference is only about 20 mV, these results would indicate that pits in group A are easier to repassivate in the aged samples. Likewise, $|E_{pit} - E_{rep}|$ slightly decreases from 182 ± 3 mV_{SCE} in the HT condition down to 146 ± 10 mV_{SCE} for sample HT1W and 156 ± 10 mV_{SCE} for HT3W. Therefore, pits in group B would be also easier to repassivate in the aged samples. However, the shift is small again, around 20–40 mV. Considering the scattering often observed in E_{pit} of aluminium alloys, further studies are required to confirm or reject the small shifts observed in $|E_{pit} - E_{ptp}|$ and $|E_{pit} - E_{rep}|$. Furthermore, a small shift of the section of the curve between E_{ptp} and E_{rep} towards higher current densities has been observed. For example, the repassivation current density (i_{rep}) value at − 825 mV_{SCE} is 12.14 ± 2.84 μA·cm^{-2} for the HT sample, 12.55 ± 2.91 μA·cm^{-2} for the HT1W and 17.32 ± 0.47 μA·cm^{-2} for HT3W. Therefore, there is a minor increase in i_{rep} when the sample is aged for 3 weeks, suggesting that this sample could contain a higher density of pits in group B.

In summary, two conclusions are obtained. Firstly, the results indicate that none of the three samples studied undergoes pitting corrosion processes during immersion at open circuit in 3.5 wt% NaCl for 1 h. Secondly, polarization curves have made it possible to establish that under aggressive conditions, two different groups of pits are formed on the samples according to their ease of repassivation.

The study of pitting during the recording of the cyclic polarization curves and the possible differences caused by the thermal ageing of Scalmalloy® samples is beyond the scope of this paper and deserves further and detailed analysis in future works.

3.4. Electrochemical impedance spectroscopy

One representative EIS spectra for each type of sample, HT, HT1W and HT3W, is displayed in Fig. 12. The modulus and impedance phase diagrams are plotted in Fig. 12 (a) and (b), while Fig. 12 (c) shows the Nyquist diagram. In addition, Fig. 12 (a), (b) and (c) include the fit of the experimental data to the equivalent electric circuit drawn in Fig. 12 (d). This circuit contains the electrical elements to model the three basic elements of the real system: the electrolyte, the passive layer, and the aluminium alloy. Thus, R_{el} is the electrolyte resistance. R_{layer} and CPE_{layer} are the resistance and a constant phase element describing the behaviour of the passive layer. R_{ct} and CPE_{ct} are related to the corrosion process of the base metal and are the charge transfer resistance and the constant phase element associated with the capacitance of the electrical double layer. Since there are heterogeneities in the structure and capacitive behaviour of the passive layer and the electrical double layer, CPEs are employed as a substitute of pure capacitors. More complex equivalent electric circuits are found in the literature to study bare aluminium alloys immersed in NaCl aqueous solutions when there are active processes associated with precipitates [60–62]. However, the electrochemical studies described in Fig. 11 and reported in our previous

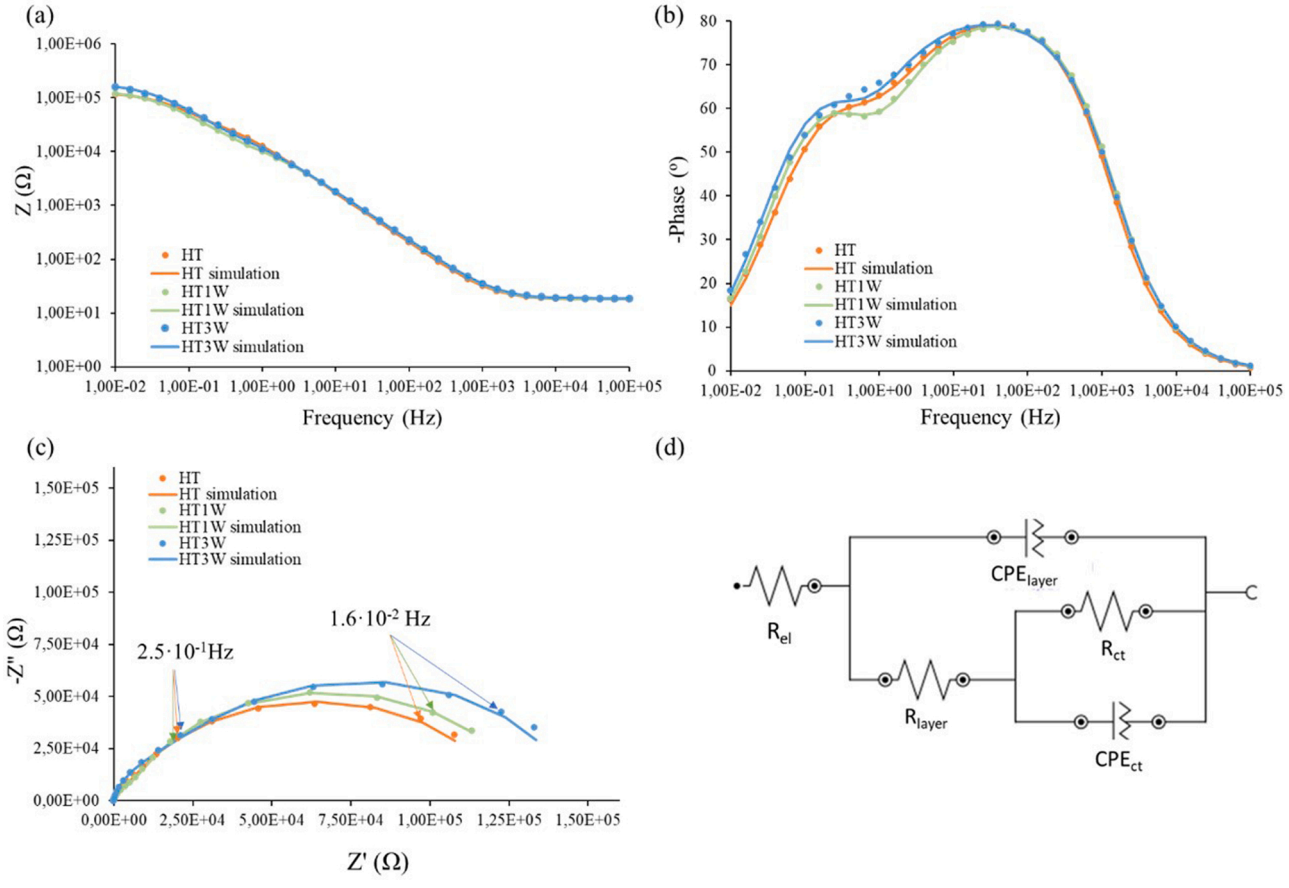

Fig. 12. EIS results of HT, HT1W and HT3W. (a) Modulus Bode plot; (b) phase angle Bode plot; (c) Nyquist plot; (d) equivalent electric circuit.

work [25] lead us to think that the activity of the precipitates during the EIS experiments is not significant. There are no transients in OCP in Fig. 11 (a), indicating there are no active pitting corrosion processes. Fig. 11 (b) shows that the alloy is in a passive state after immersion in the 3.5% NaCl solution at OCP for 1 h. Moreover, as described previously [25], we had to extend full immersion tests of bare Scalmalloy® specimens in 3.5 wt% NaCl for up to 15 days to find only small pits between 10 and 800 nm. In addition, no other features in the experimental data indicate the need for other elements to be included in the equivalent electric circuit, like warburg diffusion impedance. A comparison of the experimental and fitted values in Fig. 12 (a-c) reveals a high degree of match between them, which highlights the validity of the model proposed in Fig. 12 (d) to represent the behaviour of the system under study. Table 4 includes the EIS fitted data to the equivalent circuit together with their respective standard deviations.

The first aspect to comment regarding the curves in Fig. 12 is that they do not present inductive loops in the low-frequency region. According to [63], the presence of such loops is associated with pitting corrosion processes. Therefore, like the OCP curves, the impedance data indicate that none of the three samples undergoes pitting corrosion processes at the free corrosion potential. Moreover, when analysing the curves in Fig. 12 and the data in Table 4, there are no significant differences between the three sample types. They all exhibit capacitive behaviour associated with the passive layer, which presents a resistance of around 18–50 kΩ and a significant homogeneity since the n factor is around 0.92. In other words, based on the EIS characterisation carried out, the ageing treatment at 150 ºC for 3 weeks does not produce changes in the behaviour of the Scalmalloy® passive layer.

The behaviour of the passive layer in EIS is similar to a capacitor and Eq. 1 can be employed.

$$D = (e \cdot e^0 \cdot S)/C_{layer} \quad (1)$$

Being D the passive layer thickness, e= 10 the aluminium oxide dielectric constant, $e^0 = 8.854 \times 10^{-14}$ F·cm^{-1} the dielectric constant in vacuum, and S= 1 cm^2 the area of the sample. Provided that the n factor in CPE_{layer} is approximately 1, CPE_{layer} results in Table 4 can be employed in Eq. 1 to obtain estimations for D. Thus the passive layers of the three samples are 0.7–0.8 nm thick.

The impedance plots shown in Fig. 12, the values obtained in Table 4, and the passive layer thickness are similar to those reported by other authors when applying the equivalent electric circuit of Fig. 12 (d) to various Al-Mg alloys immersed in 3.5 wt% NaCl. Bethencourt et al. [62] performed EIS measurements on conventional AA5083 (Al-4.9Mg-0.5Mn-0.13Si-0.13Cr-0.3Fe) after being immersed in 3.5 wt % NaCl for 30 min and obtained R_{layer} = 23.26 kΩ, $CPE_{layer} = 8.75 \times 10^{-6}$ F·S$^{(n-1)}$·cm^{-2} and $n_1 = 0.934$. Since they tested 1 cm^2 of surface, applying Eq. 1 and the values e= 10 and $e^0 = 8.854 \times 10^{-14}$ F·cm^{-1}, the thickness of the passive layer is ≈ 1 nm. Mehrian et al. [64] studied AA5052 (Al-2.23Mg-0.292Fe-0.163Cr-0.147Si-0.114Mn, in wt %) after 24 h of immersion in the same corrosive medium. In this case, they obtained $R_{layer} = 12.79$ kΩ, $CPE_{layer} = 3.45 \times 10^{-6}$ F·S$^{(n-1)}$·cm^{-2} and $n_1 = 0.87483$. Applying Eq. 1 and the same values for e and e^0 as above, the thickness of the passive layer is 2.5 nm. Zhang et al. [65] built samples of Al-4.2Mg-0.4Sc-0.2Zr alloy (all in wt%), similar to Scalmalloy®, by LPBF and studied them by EIS in 3.5 wt% NaCl. The samples equivalent to those labelled here HT, subjected to a heat treatment of 325 °C for 4 h after being built, were fitted with the equivalent electric circuit in Fig. 12 (d) and they obtained values of $R_{layer} = 47.53 \pm 5.65$ kΩ, $CPE_{layer} = 1.237 \times 10^{-5}$ F·S$^{(n-1)}$·cm^{-2} and $n_1 = 0.81 \pm 0.02$. Inasmuch the studied area was 1 cm^2, their results also indicate a passive layer thickness around 0.7–0.8 nm after applying Eq.1.

3.5. Intergranular corrosion

The DoS to intergranular corrosion was measured according to the standard NAMLT procedure defined in ASTM G67–04 [26]. This standard allows for establishing the IGC behaviour of Al-Mg and Al-Mg-Mn alloys. The test is based on the determination of the mass loss experienced by the samples as a result of the selective attack of the β-phase precipitates present in the alloy caused by the aggressive acidic medium used [49], since the β-phase dissolves two orders of magnitude faster than the aluminium matrix in the NAMLT [66].

The passive layer of Al-Mg alloys is formed by oxides and hydroxides of aluminium and magnesium. However, this mixed passive layer is unstable in the very acid media of the NAMLT, which is composed of 70 vol% HNO_3. Without the proper protection of the passive layer, the potential difference between the β-phase and the aluminium matrix provides the driving force for the anodic dissolution of the β-phase precipitates along the grain boundaries according to Eqs. 2 and 3 [66].

$$Mg \rightarrow Mg^{2+} + 2e^- \quad (2)$$

$$Al \rightarrow Al^{3+} + 3e^- \quad (3)$$

The tests yielded $DoS_{HT} = 4.94 \pm 0.33$ mg·cm^{-2}, $DoS_{HT1W} = 55.15$

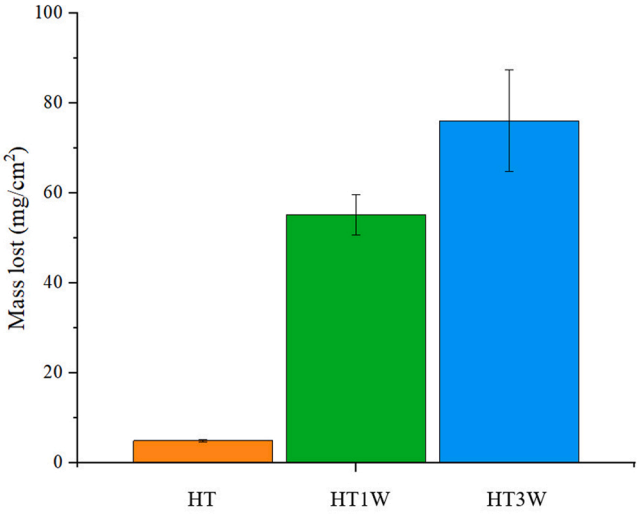

Fig. 13. Bar chart of DoS to IGC measured as the mass loss of HT, HT1W and HT3W samples after NAMLT defined in ASTM G67–04.

Table 4
EIS fitting for HT, HT1W and HT3W to the equivalent electric circuit in Fig. 12 (d).

Sample	χ^2 x 10^{-2}	R_s (Ω)	CPE_{layer} x 10^{-5} F·S$^{(n-1)}$ cm^{-2}	n_1	R_{layer} (kΩ)	CPE_{ct} x 10^{-5} F·S$^{(n-1)}$ cm^{-2}	n_2	R_{ct} (kΩ)
HT	0.95	18.45	1.21	0.92	25.17	2.36	0.86	98.27
	(± 0.06)	(± 0.41)	(± 0.11)	(± 0.01)	(± 15.52)	(± 0.56)	(± 0.06)	(± 16.19)
HT1W	0.73	18.52	1.23	0.92	33.37	1.96	0.88	141.29
	(± 0.63)	(± 0.85)	(± 0.07)	(± 0.01)	(± 23.35)	(± 0.70)	(± 0.03)	(± 10.93)
HT3W	1.28	18.54	1.17	0.92	48.29	2.01	0.89	111.40
	(± 0.62)	(± 0.41)	(± 0.07)	(± 0.01)	(± 20.46)	(± 0.43)	(± 0.02)	(± 33.73)

$\pm$ 4.53 mg·cm^{-2}, and $DoS_{HT3W} = 76.09 \pm 11.27$ mg·cm^{-2}. These results state that the treatment at 150 °C for three weeks causes the mass loss of the sample due to the intergranular corrosion process to increase by a factor of more than 15 compared to the untreated sample. In order to be able to visualise the differences between the three samples, the values obtained are shown in the form of a bar chart in Fig. 13. ASTM G67–04 classifies the samples into three categories on the basis of the mass loss suffered by the samples: (i) the material is considered resistant to IGC when the mass loss is less than 15 mg·cm^{-2}; (ii) the behaviour is considered doubtful if the values are between 15 mg·cm^{-2} and 25 mg·cm^{-2}, and metallographic examinations are then recommended to determine whether the mass loss has resulted from intergranular attack or not; and (iii) the material is IGC-sensitised if there are mass losses above 25 mg·cm^{-2}. Therefore, according to the criteria set out in ASTM G67–04 [26], Scalmalloy® manufactured under certified conditions is resistant to IGC, but artificial ageing at 150 ºC for 1 and 3 weeks produces sensitisation to IGC.

It is worth mentioning that the reproducibility of NAMLT values tends to decrease with increasing sensitization, especially at values above 25 mg·cm^{-2}, and could produce DOS values with a large error [67].

The morphology of the attack experienced by the samples during the IGC tests is analysed by means of BSE-SEM images acquired in different orientations in Fig. 14, Fig. 15 and Fig. 16. In Fig. 14, XZ planes of the samples are imaged after direct exposition to the acid etching of NAMLT. Fig. 14 (a)-(c), corresponding to the HT sample, show irregular attack in CGZ, while a more intense and uniform attack is revealed in FGZ. When comparing these images with those of sample HT1W, Fig. 14 (d)-(f), much more severe damage is observed in HT1W, with the same intensity in FGZ and CGZ. The images of HT3W, Fig. 14 (g)-(i), are similar to those obtained for HT1W, and they do not show the difference in behaviour detected by the mass loss tests.

Fig. 15 and Fig. 16 include cross-section BSE-SEM images of the samples after NAMLT in order to analyse the morphology and depth of the corrosion. Specifically, YZ-planes are imaged in Fig. 15 and XY-planes in Fig. 16. In both figures, the cross-sections of the HT sample before the test have been included as a reference. In the images corresponding to the tested HT samples, Fig. 15 (b) and Fig. 16 (b), pits between 5 and 30 μm of depth can be observed, without signs of IGC. By contrast, the existence of intergranular attack is undoubtedly observed in the samples HT1W and HT3W, Fig. 15 (c-d) and Fig. 16 (c-d), with depths reaching, approximately, 25 μm in HT1W and 30 μm in HT3W.

Zhang et al. [68] measured the DoS of Al-Mg-Mn alloys prepared by casting with different proportions of Mg and Mn and sensitised with treatments at 150 ºC for 7 days. Among the alloys studied, Al-4.28Mg-0.76Mn, with Mg and Mn contents very similar to those present in Scalmalloy®, had DoS of around 45–50 mg·cm^{-2}. This result is very similar to 55.15 $\pm$ 4.53 mg·cm^{-2} obtained here for the HT1W sample, which underwent the same sensitisation treatment. Li et al. [35] also published similar results, with mass losses $\approx$ 35 mg·cm^{-2} when ageing alloys prepared by casting with stoichiometries Al-5.8Mg-0.4Mn-0.1Sc-0.04 Zr and Al-5.8Mg-0.4Mn-0.25Sc-0.1Zr for 168 h (1 week) at 130 ºC. According to these authors, the observed mass loss is due to the formation of β-phase particles during the heat treatment and

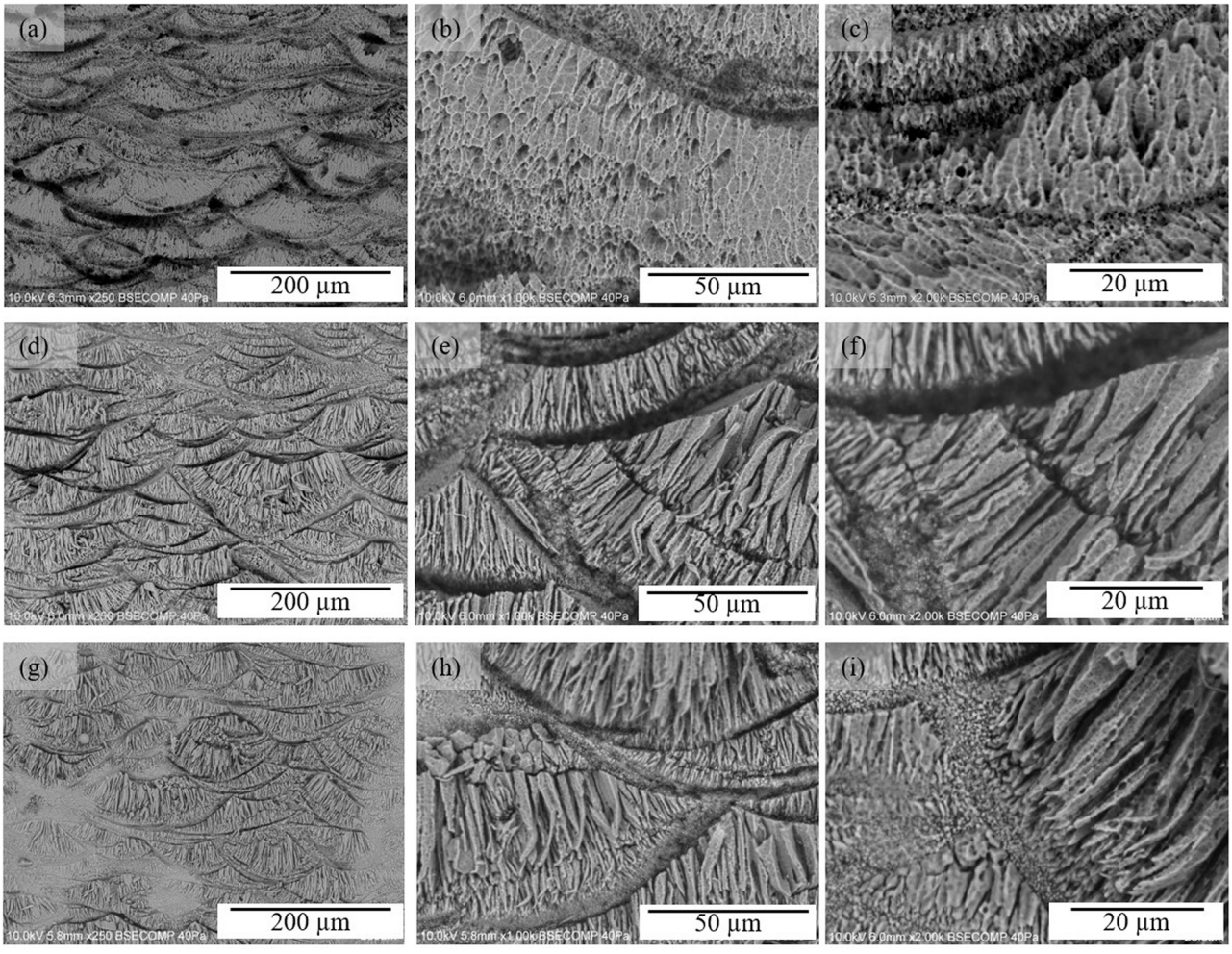

Fig. 14. BSE-SEM images of the XZ-surfaces of samples after NAMLT. (a-c) HT sample, (d-f) HT1W, and (g-i) HT3W.

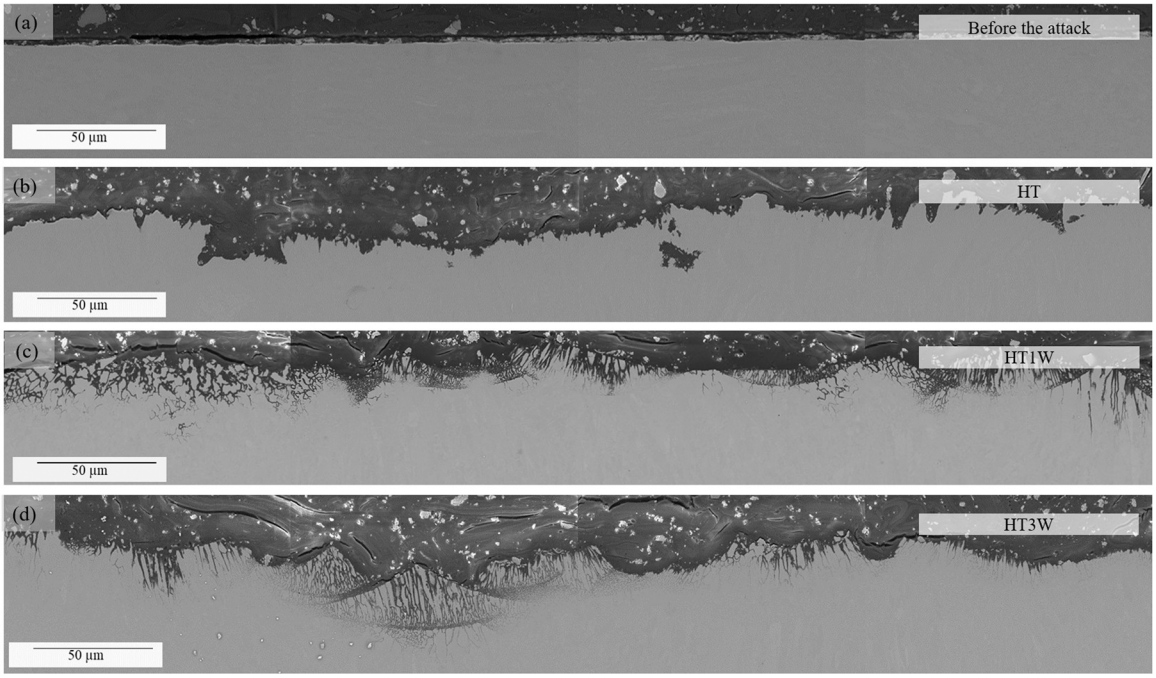

Fig. 15. BSE-SEM cross-section images of YZ-planes, close to the intersection between YZ- and XY-planes, of: (a) HT sample before NAMLT and (b) HT, (c) HT1W, and (d) HT3W samples after NAMLT.

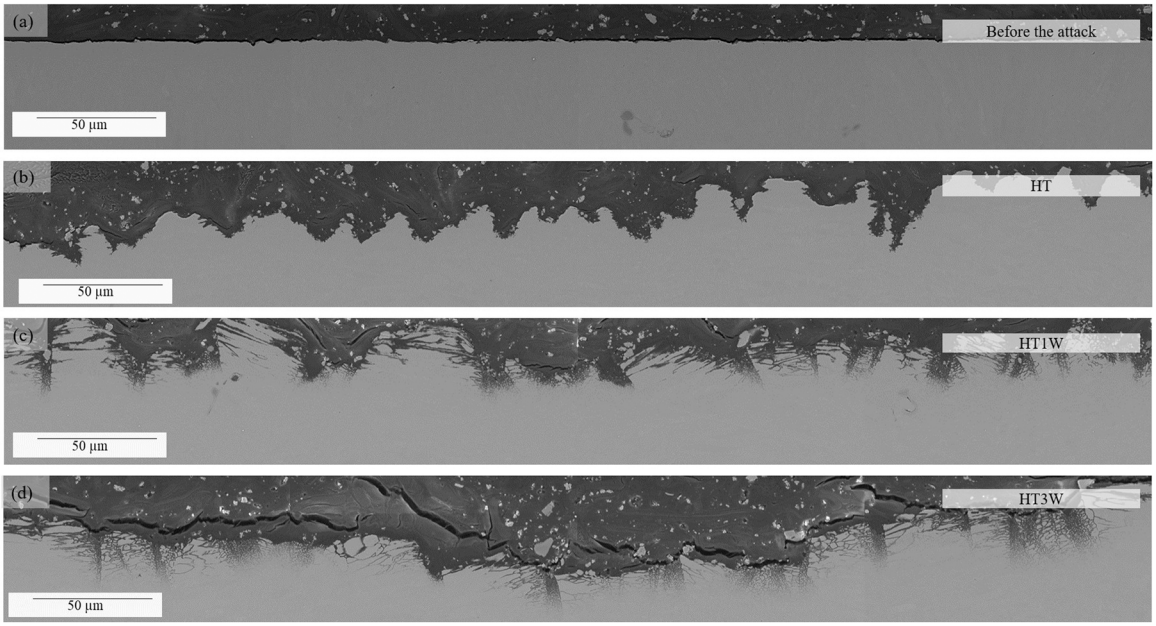

Fig. 16. BSE-SEM cross-section images of XY-planes, close to the intersection between XY- and XZ-planes, of: (a) HT sample before NAMLT and (b) HT, (c) HT1W, and (d) HT3W samples after NAMLT.

the subsequent IGC-sensitisation of the Al-5.8Mg-0.4Mn alloys.

In summary, both the mass loss and the morphology of the attack when the samples undergo the NAMLT indicate that the treatment of the Scalmalloy® samples at 150 ºC for 1 and 3 weeks causes sensitisation of the samples to IGC in a similar way to other similar Al-Mg alloys. According to the literature and the standard, the precipitation of β-phase at the grain boundaries is the origin of this sensitisation. These results are consistent with the β-phase formation revealed by STEM-EDS and persulphate etching in the preceding sections.

3.6. Stress corrosion cracking

Non-sensitised and sensitised samples were tested according to ASTM G47–98 [39] in order to study their behaviour against SCC. As described in the experimental section, the test consists of subjecting the samples to a constant load, corresponding to 80% of the yield strength, and cycles of 10 min of immersion in a 3.5 wt% NaCl solution and 50 min in air until fracture occurs or until 20 days of test without fracture. As discussed previously in Section 3.2, the differences in yield strength between HT, HT1W and HT3W are very small, approximately 1–3%, and they are attributed to small variations between samples

Table 5
Time to failure (minutes) during SCC test described in ASTM G47–98.

HT	HT1W	HT3W
28800 without fracture	193	202
28800 without fracture	68	134
28800 without fracture	501	134

rather than to real differences in their mechanical properties. Therefore, it was decided to apply 363 MPa, 80% of the yield strength for HT, to all samples in the SCC tests.

Table 5 includes the time until the facture of the samples. Firstly, it should be noted that HT samples reached the 20-day test limit without fracture. This means that HT samples withstood 480 test cycles. Contrariwise, the samples treated at 150 ºC for 1 and 3 weeks show radically different behaviour. Thus, HT1W samples exhibit a mean time to fracture of 4.2 h. Among these samples, the one with the best performance fractured during the ninth cycle, while the one with the worst behaviour fractured during the second cycle. Besides, HT3W samples showed a mean time to failure of 2.6 h. In that case, the best case fractured during the fourth cycle, while the worst sample fractured during the third cycle. In addition, the results included in Table 5 indicate that samples treated at 150 °C for 3 weeks present a more homogeneous behaviour than those treated for 1 week, as indicated by the lower variability of the results obtained.

The SE-SEM images included in Fig. 17 were recorded at different magnifications to determine the fracture surface features of HT1W and HT3W samples after the SCC tests. In this figure, images in Fig. 17 (a-c) correspond to HT1W samples while images in Fig. 17 (d-f) correspond to HT3W. Images in Fig. 10 (d) and (g), described in the previous Section 3.2 focusing on mechanical properties, display the fracture surface of HT1W and HT3W samples after being subjected to tensile tests and were acquired at the same magnification as images in Fig. 17 (a) and (d). The images after the tensile test in Fig. 10 (d) and (g) show stringencies characteristic of ductile fracture processes. Meanwhile, this striction is not observed in the images in Fig. 17 (a) and (d), indicating that HT1W and HT3W samples undergo a brittle fracture process during the SCC test. This conclusion is corroborated in the images included in Fig. 17 (b), (c), (e) and (f), in which it is observed that the fracture surfaces of the two samples present the typical cleavage aspect produced in brittle fracture processes.

SE-SEM image in Fig. 18 (a) shows an area in the fracture surface of an HT3W sample where there is a crack that initiates on the outer surface of the sample and propagates inwards perpendicularly to the applied load. Next, Fig. 18 (b) shows a BSE-SEM image of the same crack after mechanically polishing the sample. The crack is observed to propagate through both CGZ and FGZ of the sample. Finally, in the image in Fig. 18 (c), acquired at higher magnification, the intergranular character of the crack can be observed in deeper detail. It can therefore be stated that the images in Fig. 18 illustrate a process of intergranular stress corrosion cracking (IGSCC). According to [28,31], this type of intergranular fracture is characteristic of Al-Mg alloys sensitised to SCC processes.

In addition to cracks, the presence of pitting can be observed in the specimens subjected to the SCC tests. Thus, in the fracture surface of an HT3W sample displayed in Fig. 19 (a), a pit can be observed on the outer surface of the specimen, from where a crack initiated. This type of pits is also observed on the outer surface of HT specimens that did not crack during the 20-day SCC test. Fig. 19 (b) includes one of such pits. It can therefore be concluded that pitting is not a sufficient condition for sample fracture to occur during the SCC test.

The results obtained from the SCC tests show, on the one hand, that Scalmalloy® manufactured under the certified conditions established by the manufacturer features excellent behaviour against the SCC processes. On the other hand, when Scalmalloy® is aged at 150 ºC for periods of between 1 and 3 weeks, sensitisation occurs, leading to their premature failure due to brittle fracture when subjected to the SCC test defined in the ASTM G47–98 standard.

In general, it is known that SCC initiates on the surface of the material, in pre-existing defects and sites where localised corrosion occurs due to pitting or intergranular corrosion. These local defects on the surface can then evolve into cracks that grow following a variety of mechanisms such as intergranular corrosion processes, stress concentration at the crack tip, or hydrogen-assisted cracking [69–71]. The SCC process of conventional Al-Mg alloys is described in the literature as an intergranular process, i.e. IGSCC. However, up to date, no data are describing this type of phenomenon in Scalmalloy® or other Al-Mg-Sc-Zr alloys manufactured by LPBF. For Al-Mg alloys, an SCC mechanism comprising two stages has been proposed: anodic dissolution of the β-phase and hydrogen embrittlement [28,29,31,72,73].

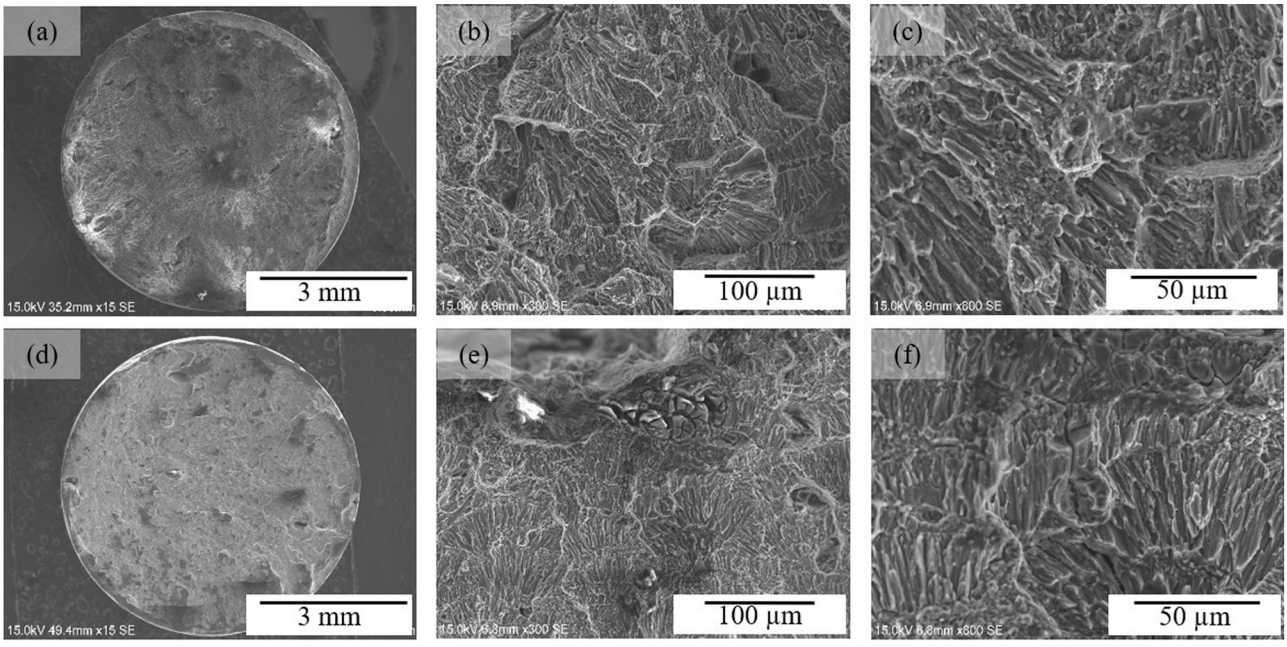

Fig. 17. SE-SEM images of fracture surfaces after SCC test according to ASTM G47–98. (a-c) HT1W, (d-f) HT3W.

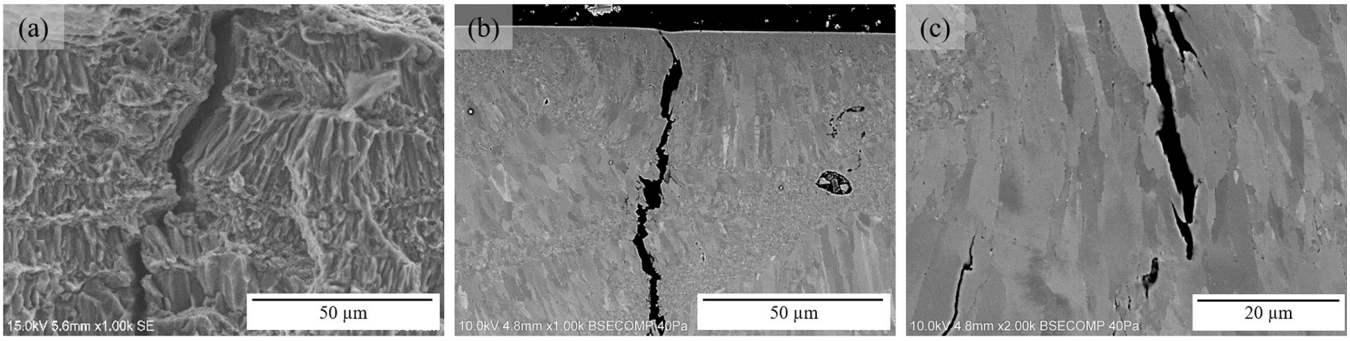

Fig. 18. (a) Fracture surface of an HT3W sample after SCC test; (b) and (c) BSE-SEM images of the crack observed in image (a) after polishing the surface.

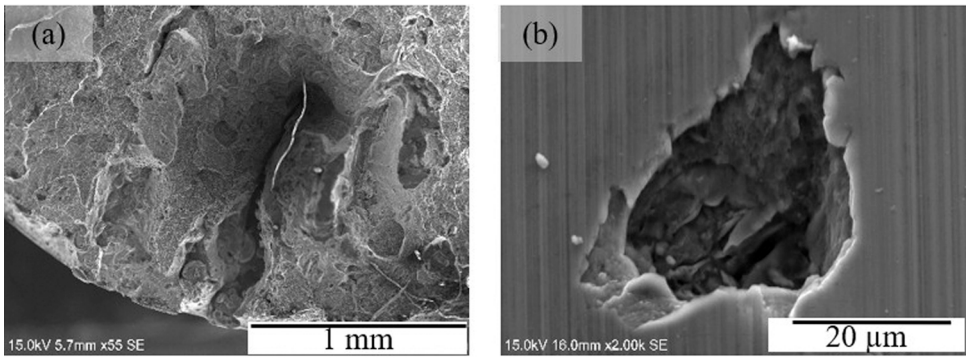

Fig. 19. (a) Pit and associated crack on the fracture surface of an HT3W specimen after SCC test. (b) Pit on the outer surface of an HT specimen after SCC test.

Hence, intergranular fracture occurs when the grain boundaries are weakened by selective dissolution of the anodic β-phase at the grain boundaries and the hydrogen diffuses towards these grain boundaries.

The anodic character of the β-phase with respect to Al-Mg matrices is based on the value of its electrochemical potential, which presents values between − 1100 and − 1300 mV_{SCE} and a pitting potential of ≈ −950 mV_{SCE} in 3.5 wt% NaCl [28,31,54,55]. Thus, as explained by Argade et al. [28] for an alloy such as 5083, which has a free corrosion potential of ≈ −760 mV_{SCE}, there is a large potential difference between the β-phase and the Al-Mg matrix, originating a strong galvanic couple that results in the consequent dissolution of the β-phase. For Scalmalloy®, the free corrosion potential is ≈ −1100 mV_{SCE} [25]. Provided that β-phase forms in sensitised Scalmalloy® samples, it will also form a galvanic couple, although weaker than that formed in samples of alloy 5083. In the section dedicated to the discussion of the cyclic polarization curves, we indicated that the β-phase is passivated at the Scalmalloy® free corrosion potential, thus justifying the fact that no pitting is evidenced during the 1-hour OCP records. However, the immersion times are much longer than 1 h in the SCC tests and, in addition, the aggressiveness of the test increases as a result of the wetting/drying cycles. Under these conditions, it seems reasonable to assume that the degradation of the β-phase passive layer and its dissolution are facilitated. Then, the anodic reactions of Al and Mg oxidation described in Eqs. 2 and 3 will take place [73]:

Possible cathodic reactions accompanying the anodic reactions are the hydrolysis of water, Eq. 4 [29,72] and proton reduction, Eq. 5 [29,73]:

$$H_2O + e^- \rightarrow OH^- + H \quad (4)$$

$$2\,H^+ + 2\,e^- \rightarrow 2\,H \quad (5)$$

Moreover, Al^{3+} and Mg^{2+} cations are hydrolised, producing H^+ according to Eqs. 6 and 7 [29,73]:

$$Al^{3+} + H_2O \rightarrow AlOH^{2+} + H^+ \quad (6)$$

$$Mg^{2+} + H_2O \rightarrow MgOH^+ + H^+ \quad (7)$$

The evolved hydrogen due to the described reactions in Eqs. 4 to 7 may adsorb at the crack tip, followed by absorption. Once the hydrogen atoms have entered the aluminium structure, they can diffuse to and along the grain boundaries ahead of the crack tip aided by the presence of dislocations adjacent to the grain boundaries [74]. Then, hydrogen embrittlement is produced at the grain boundaries, favouring grain boundaries decohesion where there is a discontinuity between one β-phase particle and another. In addition, the local pH decrease produced by the hydrolysis of Al^{3+} and Mg^{3+}, Eqs. 6 and 7, promotes the migration of Cl^- anions to the crack tip for charge neutralization. In turn, Cl^- anions produce subsequent attacks to the passive layer and aluminium matrix oxidation, further fostering the crack tip acidification.

The assistance of hydrogen in the SCC of Al-Mg alloys is further supported by several findings. The kinetics of IGSCC is not explained only with the anodic dissolution of the β-phase because IGSCC proceeds orders of magnitude faster than IGC [75–78] and models to predict fracture behaviour based on hydrogen-enhanced decohesion (HEDE) are successfully applied [29,79,80].

In addition to the locally formed hydrogen, there are other possible sources of hydrogen when testing SCC. Hirayama et al. [72] have analysed in detail how both the hydrogen previously present in the alloy and the external hydrogen that can be introduced from the surrounding medium contribute to the stress corrosion cracking process, confirming previous results published by other authors [78,81–83]. Thus, for example, pre-existing hydrogen in the alloy can be found because the passive layer of Al-Mg alloys is more permeable to hydrogen diffusion than others and the solubility of hydrogen in Al-Mg alloys is higher than in aluminium. A second route of hydrogen incorporation is intentional addition. Hence, Oger et al. [69] charged with hydrogen specimens of AA7046 before the SCC tests by immersing the samples in aqueous

solutions for a certain time. Bhuiyan et al. [84] cathodically charged hydrogen in AA7150 when using electro discharge machining (EDM). A third source of hydrogen is the vapour of H_2O present in the humid air during the SCC test. The passive oxide layer on the surface of the aluminium alloy can be damaged during the external loading and the reaction between atmospheric water and aluminium produces hydrogen which enters the aluminium alloy structure [72,85].

It is also worth mentioning that the presence of Mg as the major alloy element could also have a synergistic effect with hydrogen embrittlement. Hydrogen preferentially reacts with magnesium rather than with aluminium to form magnesium hydride. Hence, several authors suggest [86–88] that the segregation of magnesium along the grain boundaries enhances the amount of absorbed hydrogen, leading to hydrogen embrittlement. According to the characterization described previously, there is no evidence of β-phase nor Mg segregation at the grain boundaries in the microstructure of the unsensitised alloy, only small and dispersed Mg-rich precipitates are observed at the grain boundaries in Fig. 5 and Fig. 6. Contrariwise, large Mg segregation is observed in the sensitised samples, Fig. 5 and Fig. 6, mainly attributed to β-phases.

The described mechanisms of IGSCC in conventional Al-Mg alloys are plausible to also operate in Scalmalloy® but additional studies are required to understand the SCC behaviour of Scalmalloy® and similar aluminium alloys processed by LPBF.

4. Conclusions

The work described here provide for the first time information about the effect of temperature on the in-service behaviour of Scalmalloy® parts manufactured using LPBF. The corrosion performance and mechanical properties of the certified material (HT) and after applying 150 ºC for 1 (HT1W) and 3 weeks (HT3W) were studied.

The most important conclusion drawn is that Scalmalloy® manufactured under certified conditions is both IGC- and SCC-resistant, but the exposition to temperatures close to 150 ºC produces the formation of β-phase Al_3Mg_2 at the grain boundaries, which in turn originates the degradation of the material's properties when it is exposed to a corrosive environment.

The main conclusions of the study are as follows:

- No significant differences are observed by BSE-SEM between the three types of samples in the bimodal microstructure formed by FGZ and CGZ, and their corresponding grain sizes and factor shapes.
- After the thermal sensitisation, the formation of new and/or coarsening of pre-existing Sc-rich particles and the precipitation of intergranular Mg-rich phases are evidenced by STEM-EDS analyses. Sc-rich particles are attributed to $Al_3(Sc_{1-x},Zr_x)$ phases and Mg-rich phases to β-phase Al_3Mg_2. The development of a β-phase network along the grain boundaries is also supported by etching in acidified 0.4 M $(NH_4)_2S_2O_8$ solution.
- Tensile tests according to ASTM E8/ E8M and hardness tests according to ASTM E384 indicate that the sensitisation treatment does not significantly affect the mechanical properties of the material. Ductile fractures are exhibited by the three types of specimens and the approximate values measured are: E ≈ 66 GPa, RP ≈ 460 MPa, RT ≈ 521 MPa, elongation ≈ 12%, reduction of area ≈ 17%, and Vickers hardness 164 HV.
- Open circuit potential (OCP) and EIS measurements after 1 h of immersion in 3.5 wt% NaCl indicate the absence of pitting phenomena at the free corrosion potential during this exposure time.
- From the cyclic polarization study performed in 3.5 wt% NaCl it is established that there are no drastic modifications in the pitting corrosion of Scalmalloy® when subjected to the thermal sensitisation. All conditions show a passivity zone in the forward scan, a pitting potential (E_{pit}) and the complete repassivation of pits in the reverse scan. Likewise, a pitting transition potential (E_{ptp}) is defined in the reverse scan, indicating the existence of two sets of pits featuring different repassivation abilities.
- According to EIS results, all three types of samples exhibit capacitive behaviour associated with a passive layer of 0.7–0.8 nm of thickness, and the ageing treatment at 150 ºC for 3 weeks does not produce changes in the behaviour of the Scalmalloy® passive layer.
- Scalmalloy® manufactured under certified conditions is resistant to IGC according to the criteria set out in ASTM G67-04 and the measurements made by the Nitric acid mass loss test (NMALT), with $DoS_{HT} = 4.94 \pm 0.33$ mg·cm^{-2}. However, the exposure to 150 ºC for 1 and 3 weeks produces sensitisation of HT1W and HT3W conditions to IGC caused by the aforementioned development of a β-phase network along the grain boundaries. Hence, $DoS_{HT1W} = 55.15 \pm 4.53$ mg·cm^{-2}, and $DoS_{HT3W} = 76.09 \pm 11.27$ mg·cm^{-2}.
- HT condition is SCC-resistant when tested following ASTM G47-98, but the sensitization heat treatment produces SCC-sensitisation attributed to the formation of intergranular β-phase. Thus, HT1W and HT3W conditions show premature brittle and intergranular stress corrosion cracking (IGSCC) during the first hours of test that initiates in pits formed in the outer surface of the specimens tested.

These results warn about the limitation of Scalamlloy® to be employed in service conditions involving exposure to temperatures close to 150 ºC. Furthermore, they encourage the scientific community to develop strategies to avoid or minimise the formation of the Al_3Mg_2 precipitates, such as new chemical formulations, manufacturing parameters or thermo-mechanical post-treatments.

CRediT authorship contribution statement

L.C.C.: Data curation; Investigation; Writing – original draft; Writing – review & editing. **L.G.R.:** Conceptualization; Funding acquisition; Data curation; Writing – original draft; Writing – review & editing. **J.L.C.:** Data curation; Investigation. **A.O.L:** Investigation. F.**J.B.:** Conceptualization; Funding acquisition; Methodology; Supervision; Writing – review & editing.

Declaration of Competing Interest

The authors declare that they have no known competing financial interests or personal relationships that could have appeared to influence the work reported in this paper.

Data availability

The raw/processed data required to reproduce these findings cannot be shared at this time as the data also forms part of an ongoing study.

Acknowledgments

SEM and TEM data were obtained at SC-ICYT University of Cadiz. L. G.R. acknowledges support from the Programme for Attracting Talent of UCA and from IMEYMAT: Institute of Research on Electron Microscopy and Materials, UCA. L.C.C. and A.O.L. acknowledge support from UCA and Titania, Ensayos y Proyectos Industriales S.L for their predoctoral positions. The authors would also like to acknowledge Titania, Ensayos y Proyectos Industriales S.L. for the support in the achievements of this work.

References

[1] A. Aversa, G. Marchese, A. Saboori, E. Bassini, D. Manfredi, S. Biamino, D. Ugues, P. Fino, M. Lombardi, New aluminum alloys specifically designed for laser powder bed fusion: a review, Materials 12 (2019), https://doi.org/10.3390/ma12071007.
[2] J.H. Martin, B.D. Yahata, J.M. Hundley, J.A. Mayer, T.A. Schaedler, T.M. Pollock, 3D printing of high-strength aluminium alloys, Nature 549 (2017) 365–369, https://doi.org/10.1038/nature23894.

[3] P.A. Rometsch, Y. Zhu, X. Wu, A. Huang, Review of high-strength aluminium alloys for additive manufacturing by laser powder bed fusion, Mater. Des. 219 (2022), 110779, https://doi.org/10.1016/j.matdes.2022.110779.

[4] Z. Hu, X. Nie, Y. Qi, H. Zhang, H. Zhu, Cracking criterion for high strength Al–Cu alloys fabricated by selective laser melting, Addit. Manuf. 37 (2021), 101709, https://doi.org/10.1016/j.addma.2020.101709.

[5] H. Hyer, L. Zhou, S. Park, T. Huynh, A. Mehta, S. Thapliyal, R.S. Mishra, Y. Sohn, Elimination of extraordinarily high cracking susceptibility of aluminum alloy fabricated by laser powder bed fusion, J. Mater. Sci. Technol. 103 (2022) 50–58, https://doi.org/10.1016/j.jmst.2021.06.023.

[6] J. Fu, H. Li, X. Song, M.W. Fu, Multi-scale defects in powder-based additively manufactured metals and alloys, J. Mater. Sci. Technol. 122 (2022) 165–199, https://doi.org/10.1016/j.jmst.2022.02.015.

[7] A.B. Spierings, Powder Spread Charact. Sc. - Zr-Modif. Alum. Alloy. Process. Sel. Laser Melting (2018), https://doi.org/10.3929/ethz-b-000253924.

[8] K. Schmidtke, F. Palm, A. Hawkins, C. Emmelmann, Process and mechanical properties: applicability of a scandium modified Al-alloy for laser additive manufacturing, Phys. Procedia 12 (2011) 369–374, https://doi.org/10.1016/j.phpro.2011.03.047.

[9] M. Awd, J. Tenkamp, M. Hirtler, S. Siddique, M. Bambach, F. Walther, Comparison of microstructure and mechanical properties of Scalmalloy® produced by selective laser melting and laser metal deposition, Materials 11 (2017), https://doi.org/10.3390/ma11010017.

[10] A.B. Spierings, K. Dawson, T. Heeling, P.J. Uggowitzer, R. Schäublin, F. Palm, K. Wegener, Microstructural features of Sc- and Zr-modified Al-Mg alloys processed by selective laser melting, Mater. Des. 115 (2017) 52–63, https://doi.org/10.1016/j.matdes.2016.11.040.

[11] J.A. Glerum, C. Kenel, T. Sun, D.C. Dunand, Synthesis of precipitation-strengthened Al-Sc, Al-Zr and Al-Sc-Zr alloys via selective laser melting of elemental powder blends, Addit. Manuf. 36 (2020), 101461, https://doi.org/10.1016/j.addma.2020.101461.

[12] A.B. Spierings, K. Dawson, K. Kern, F. Palm, K. Wegener, SLM-processed Sc- and Zr-modified Al-Mg alloy: Mechanical properties and microstructural effects of heat treatment, Mater. Sci. Eng. A 701 (2017) 264–273, https://doi.org/10.1016/j.msea.2017.06.089.

[13] J. Musekamp, T. Reiber, H.C. Hoche, M. Oechsner, M. Weigold, E. Abele, Influence of LPBF-surface characteristics on fatigue properties of Scalmalloy®, Metals 11 (2021) 1961, https://doi.org/10.3390/met11121961.

[14] X.F. Shen, Z.Y. Cheng, C.G. Wang, H.F. Wu, Q. Yang, G.W. Wang, S.K. Huang, Effect of heat treatments on the microstructure and mechanical properties of Al-Mg-Sc-Zr alloy fabricated by selective laser melting 143 (2021), https://doi.org/10.1016/j.optlastec.2021.107312.

[15] R. Jones, J. Cizek, O. Kovarik, A. Ang, V. Champagne, Observations on comparable aluminium alloy crack growth curves: additively manufactured Scalmalloy® as an alternative to AA5754 and AA6061-T6 alloys, Addit. Manuf. Lett. 2 (2022), 100026, https://doi.org/10.1016/j.addlet.2022.100026.

[16] A.B. Spierings, K. Dawson, P.J. Uggowitzer, K. Wegener, Influence of SLM scan-speed on microstructure, precipitation of Al3Sc particles and mechanical properties in Sc- and Zr-modified Al-Mg alloys, Mater. Des. 140 (2018) 134–143, https://doi.org/10.1016/j.matdes.2017.11.053.

[17] D. Koutny, D. Skulina, L. Pantělejev, D. Paloušek, B. Lenczowski, F. Palm, A. Nick, Processing of Al-Sc aluminum alloy using SLM technology, Procedia CIRP 74 (2018) 44–48, https://doi.org/10.1016/j.procir.2018.08.027.

[18] F. Lasagni, C. Galleguillos, M. Herrera, J. Santaolaya, D. Hervás, S. González, A. Periñán, On the processability and mechanical behavior of Al–Mg–Sc alloy for PBF-LB, Prog. Addit. Manuf. 7 (2021) 29–39, https://doi.org/10.1007/s40964-021-00216-z.

[19] L. Cabrera-Correa, L. González-Rovira, J. de Dios López-Castro, M. Castillo-Rodríguez, F.J. Botana, Effect of the heat treatment on the mechanical properties and microstructure of Scalmalloy® manufactured by Selective Laser Melting (SLM) under certified conditions, Mater. Charact. (2022), 112549, https://doi.org/10.1016/j.matchar.2022.112549.

[20] S. Begoc, F. Montredon, G. Pommatau, G. Leger, M. Gas, Additive manufacturing of Scalmalloy ® satellite parts, 8Th European Conference for Aeronautics and Space Sciences (Eucass). (2019) 1–15. https://doi.org/10.13009/EUCASS2019–677.

[21] C. Digital, This company wants to electrify the world of drag racing, Create. (2018) (Acces 01/12/2022). ⟨https://createdigital.org.au/company-electrify-world-drag-racing/⟩.

[22] I.M.B., New M.T.B. Frame – Ligther Than Titanium, Less Fragile Than Carbon, (2017) Access 01/12/2022. ⟨https://www.imbikemag.com/mountain-bike-news/2017/06/new-mtb-frame-ligther-than-titanium-less-fragile-than-carbon/⟩.

[23] F. Kuisat, F. Ränke, R. Baumann, F. Lasagni, A.F. Lasagni, Fabrication of water- and ice-repellent surfaces on additive-manufactured components using laser-based microstructuring methods, Adv. Eng. Mater. 24 (2022), https://doi.org/10.1002/adem.202101624.

[24] P. Astola-González, R. Páez, J.W. Cóndor, J.M. Moreno-López, L. González-Rovira, A. Ojeda-López, Additive manufacturing for the optimization of satellite horizon sensors, in: Book of Abstract 16th CNMAT, 2022, Sociedad Española de Materiales, 2022, pp. 195–196.

[25] L. Cabrera-Correa, L. González-Rovira, J.D. López-Castro, F.J. Botana, Pitting and intergranular corrosion of Scalmalloy® aluminium alloy additively manufactured by Selective Laser Melting (SLM), Corros. Sci. (2022) 1–16, https://doi.org/10.1016/j.corsci.2022.110273.

[26] ASTM G67-04 Standard Test Method for Determining the Susceptibility to Intergranular Corrosion of 5XXX Series Aluminum Alloys by Mass Loss After Exposure to Nitric Acid (NAMLT Test). http://doi.org/10.1520/G0067-04.

[27] J. Ress, U. Martin, J. Bosch, R.K. Gupta, D.M. Bastidas, Intergranular to intragranular pitting corrosion transition mechanism of sensitized aa5083 at 150°c, Met. (Basel) 10 (2020) 1–21, https://doi.org/10.3390/met10081082.

[28] G.R. Argade, N. Kumar, R.S. Mishra, Stress corrosion cracking susceptibility of ultrafine grained Al-Mg-Sc alloy, Mater. Sci. Eng. A 565 (2013) 80–89, https://doi.org/10.1016/j.msea.2012.11.066.

[29] C.B. Crane, R.P. Gangloff, Stress corrosion cracking of Al-Mg alloy 5083 sensitized at low temperature, Corrosion 72 (2016) 221–241, https://doi.org/10.5006/1766.

[30] J. Gao, D.J. Quesnel, Enhancement of the stress corrosion sensitivity of AA5083 by heat treatment, Met. Mater. Trans. A Phys. Met. Mater. Sci. 42 (2011) 356–364, https://doi.org/10.1007/s11661-010-0375-3.

[31] J.L. Searles, P.I. Gouma, R.G. Buchheit, Stress corrosion cracking of sensitized AA5083 (Al-4.5Mg-1.0Mn), Mater. Sci. Forum 396– 402 (2002) 1437–1442, https://doi.org/10.4028/www.scientific.net/msf.396-402.1437.

[32] R. Zhang, M.A. Steiner, S.R. Agnew, S.K. Kairy, C.H.J. Davies, N. Birbilis, Experiment-based modelling of grain boundary β-phase (Mg2Al3) evolution during sensitisation of aluminium alloy AA5083, Sci. Rep. 7 (2017) 1–14, https://doi.org/10.1038/s41598-017-03090-4.

[33] R. Goswami, G. Spanos, P.S. Pao, R.L. Holtz, Precipitation behavior of the β phase in Al-5083, Mater. Sci. Eng. A 527 (2010) 1089–1095, https://doi.org/10.1016/j.msea.2009.10.007.

[34] J. Yan, A.M. Hodge, Study of β precipitation and layer structure formation in Al 5083: The role of dispersoids and grain boundaries, J. Alloy. Compd. 703 (2017) 242–250, https://doi.org/10.1016/j.jallcom.2017.01.360.

[35] M. jia Li, S. Liu, X. dong Wang, Y. jia Shi, Q. lin Pan, X. jie Zhou, R. feng Zhang, N. Birbilis, Improved intergranular corrosion resistance of Al-Mg-Mn alloys with Sc and Zr additions, Micron 154 (2022), 103202, https://doi.org/10.1016/j.micron.2021.103202.

[36] Y. Qiu, X. Yang, J. Li, S. Xiang, J. Shi, J. Xu, R.E. Sanders, The influence of Sc and Zr additions on microstructure and corrosion behavior of AA5182 alloy sheet, Corros. Sci. 199 (2022), 110181, https://doi.org/10.1016/j.corsci.2022.110181.

[37] ASTM E8/E8M standard test methods for tension testing of metallic materials. http://doi.org/10.1520/E0008_E0008M-22.

[38] ASTM E384 Standard test method for microindentation hardness of materials. http://doi.org/10.1520/E0384-22.

[39] ASTM G47-98Standard Test Method for Determining Susceptibility to Stress-Corrosion Cracking of 2xxx and 7xxx Aluminium Alloy Products.http://doi.org/10.1520/G0047-98.

[40] C.N. Kuo, P.C. Peng, D.H. Liu, C.Y. Chao, Microstructure evolution and mechanical property response of 3D-printed scalmalloy with different heat-treatment times at 325◦C, Metals 11 (2021), https://doi.org/10.3390/met11040555.

[41] J.P. Isaac, S. Lee, N. Shamsaei, H.V. Tippur, Dynamic fracture behavior of additively manufactured Scalmalloy®: Effects of build orientation, heat-treatment and loading-rate, Mater. Sci. Eng. A 826 (2021), 141978, https://doi.org/10.1016/j.msea.2021.141978.

[42] D. Gu, H. Zhang, D. Dai, C. Ma, H. Zhang, Y. Li, S. Li, Anisotropic corrosion behavior of Sc and Zr modified Al-Mg alloy produced by selective laser melting, Corros. Sci. 170 (2020), 108657, https://doi.org/10.1016/j.corsci.2020.108657.

[43] R. Li, M. Wang, T. Yuan, B. Song, C. Chen, K. Zhou, P. Cao, Selective laser melting of a novel Sc and Zr modified Al-6.2 Mg alloy: Processing, microstructure, and properties, Powder Technol. 319 (2017) 117–128, https://doi.org/10.1016/j.powtec.2017.06.050.

[44] T. Dorin, M. Ramajayam, A. Vahid, T. Langan, Chapter 12: Aluminium Scandium Alloys. Fundamentals of Aluminium Metallurgy, Elsevier Ltd,, 2018, pp. 439–494, https://doi.org/10.1016/b978-0-08-102063-0.00012-6.

[45] G. Yi, W. Zeng, J.D. Poplawsky, D.A. Cullen, Z. Wang, M.L. Free, Characterizing and modeling the precipitation of Mg-rich phases in Al 5xxx alloys aged at low temperatures, J. Mater. Sci. Technol. 33 (2017) 991–1003, https://doi.org/10.1016/j.jmst.2017.02.001.

[46] D. Scotto D'Antuono, J. Gaies, W. Golumbfskie, M.L. Taheri, Direct measurement of the effect of cold rolling on β phase precipitation kinetics in 5xxx series aluminum alloys, Acta Mater. 123 (2017) 264–271, https://doi.org/10.1016/j.actamat.2016.10.060.

[47] M. Šlapáková, B. Křivská, J. Bajer, O. Grydin, M. Stolbchenko, M. Cieslar, Transmission electron microscopy study of microstructure evolution of Al-Mg-Sc alloy after annealing at 120◦C, Acta Phys. Pol. A 134 (2018) 871–875, https://doi.org/10.12693/APhysPolA.134.871.

[48] J. Buczynski Electrochemical Analyses of Etchants Used to Detect Sensitization in Marine-Grade 5XXX Aluminum-Magnesium Alloys 2012 University of Virginia. https://doi.org/10.18130/V3QH2R.

[49] Y.K. Yang, T. Allen, Direct visualization of β phase causing intergranular forms of corrosion in Al-Mg alloys, Mater. Charact. 80 (2013) 76–85, https://doi.org/10.1016/j.matchar.2013.03.014.

[50] M.K. Cavanaugh, N. Birbilis, R.G. Buchheit, F. Bovard, Investigating localized corrosion susceptibility arising from Sc containing intermetallic Al3Sc in high strength Al-alloys, Scr. Mater. 56 (2007) 995–998, https://doi.org/10.1016/j.scriptamat.2007.01.036.

[51] J. Wloka, S. Virtanen, Influence of scandium on the pitting behaviour of Al-Zn-Mg-Cu alloys, Acta Mater. 55 (2007) 6666–6672, https://doi.org/10.1016/j.actamat.2007.08.021.

[52] Z. Tang, F. Jiang, P. Xu, J. Jiang, J. Zeng, L. Lu, M. Tong, Investigation on microstructure, mechanical properties and corrosion behavior of VPPA welded Al–Mg–Mn–Sc–Zr alloy, Mater. Today Commun. 25 (2020), 101480, https://doi.org/10.1016/j.mtcomm.2020.101480.

[53] Z. Ahmad, A. Ul-Hamid, A.A. B.j, The corrosion behavior of scandium alloyed Al 5052 in neutral sodium chloride solution, Corros. Sci. 43 (2001) 1227–1243, https://doi.org/10.1016/S0010-938X(00)00147-5.
[54] J.A. Lyndon, R.K. Gupta, M.A. Gibson, N. Birbilis, Electrochemical behaviour of the β-phase intermetallic (Mg2Al3) as a function of pH as relevant to corrosion of aluminium-magnesium alloys, Corros. Sci. 70 (2013) 290–293, https://doi.org/10.1016/j.corsci.2012.12.022.
[55] N. Birbilis, R.G. Buchheit, Electrochemical characteristics of intermetallic phases in aluminum alloys, J. Electrochem Soc. 152 (2005) B140–B151, https://doi.org/10.1149/1.1869984.
[56] R. Parvizi, M.Y. Tan, A.E. Hughes, Recent Insights Into Corrosion Initiation at the Nanoscale, in: R.N. Lumley (Ed.). Fundamentals of Aluminium Metallurgy, Woodhead P,, 2018, pp. 525–551, https://doi.org/10.1016/B978-0-08-102063-0.00014-X ©.
[57] J. Li, J. Dang, A summary of corrosion properties of Al-Rich solid solution and secondary phase particles in al alloys, in: Metals (Basel), 7, 2017, pp. 3–5, https://doi.org/10.3390/met7030084.
[58] S. Jain, M.L.C. Lim, J.L. Hudson, J.R. Scully, Spreading of intergranular corrosion on the surface of sensitized Al-4.4Mg alloys: a general finding, Corros. Sci. 59 (2012) 136–147, https://doi.org/10.1016/j.corsci.2012.02.018.
[59] S. Esmailzadeh, M. Aliofkhazraei, H. Sarlak, Interpret. Cycl. Potentiodynamic Polariz. Test. Results Study Corros. Behav. Met.: A Rev. 1 (54) (2018) 976–989, https://doi.org/10.1134/S207020511805026X.
[60] M. Bethencourt, F.J. Botana, M.J. Cano, M. Marcos, J.M. Sánchez-Amaya, L. González-Rovira, Behaviour of the alloy AA2017 in aqueous solutions of NaCl. Part I: Corrosion mechanisms, Corros. Sci. 51 (2009) 518–524, https://doi.org/10.1016/j.corsci.2008.12.027.
[61] F.J. Botana, A. Aballe, M. Bethencourt, M.J. Cano, M. Marcos, On the mixed nature of cerium conversion coatings U È ber die Eigenschaften von Cer-Umwandlungsschichten, Mater. Corros. 53 (2023) 176–184, https://doi.org/10.1002/1521-4176(200203)53:3<176::AID-MACO176>3.0.CO;2-K.
[62] M. Bethencourt, F.J. Botana, M.J. Cano, M. Marcos, J.M. Sánchez-Amaya, L. González-Rovira, Using EIS to analyse samples of Al-Mg alloy AA5083 treated by thermal activation in cerium salt baths, Corros. Sci. 50 (2008) 1376–1384, https://doi.org/10.1016/j.corsci.2007.12.009.
[63] A. Aballe, M. Bethencourt, F.J. Botana, M. Marcos, M.A. Rodríguez-Chacón, Seguimiento de la corrosión de la aleación AA2024 en disoluciones de NaCl mediante la medida del ruido electroquímico, Rev. De. Metal. 34 (1998) 42–46, https://doi.org/10.3989/revmetalm.1998.v34.iextra.705.
[64] S.S.M. Mehrian, M. Rahsepar, F. Khodabakhshi, A.P. Gerlich, Effects of friction stir processing on the microstructure, mechanical and corrosion behaviors of an aluminum-magnesium alloy, Surf. Coat. Technol. 405 (2021), 126647, https://doi.org/10.1016/j.surfcoat.2020.126647.
[65] H. Zhang, D. Gu, D. Dai, C. Ma, Y. Li, M. Cao, S. Li, Influence of heat treatment on corrosion behavior of rare earth element Sc modified Al-Mg alloy processed by selective laser melting, Appl. Surf. Sci. 509 (2020), 145330, https://doi.org/10.1016/j.apsusc.2020.145330.
[66] M. Lyn, C. Lim, R.G. Kelly, J.R. Scully, Overview of Intergranular Corrosion Mechanisms, Phenomenological Observations, and Modeling of AA5083, Corrosion 72 (2016) 198–220, https://doi.org/10.5006/1818.
[67] M.A. Steiner, S.R. Agnew, Modeling sensitization of Al-Mg alloys via β-phase precipitation kinetics, Scr. Mater. 102 (2015) 55–58, https://doi.org/10.1016/j.scriptamat.2015.02.012.
[68] R. Zhang, J. Li, Q. Li, Y. Qi, Z. Zeng, Y. Qiu, X. Chen, S.K. Kairy, S. Thomas, N. Birbilis, Analysing the degree of sensitisation in 5xxx series aluminium alloys using artificial neural networks: A tool for alloy design, Corros. Sci. 150 (2019) 268–278, https://doi.org/10.1016/j.corsci.2019.02.003.
[69] L. Oger, E. Andrieu, G. Odemer, L. Peguet, C. Blanc, Hydrogen - dislocation interactions in a low-copper 7xxx aluminium alloy: About the analysis of interrupted stress corrosion cracking tests, Mater. Sci. Eng. A 790 (2020), https://doi.org/10.1016/j.msea.2020.139654.
[70] M. Bobby Kannan, P. Bala Srinivasan, V.S. Raja, Stress corrosion cracking (SCC) of aluminium alloys, in: Stress Corrosion Cracking: Theory and Practice, Elsevier Ltd, 2011, pp. 307–340, https://doi.org/10.1533/9780857093769.3.307.
[71] T.D. Burleigh, Postulated mechanisms for stress corrosion cracking of aluminum alloys. A review of the literature 1980-1989, Corrosion 47 (1991) 89–98, https://doi.org/10.5006/1.3585235.
[72] K. Hirayama, H. Toda, D. Fu, R. Masunaga, H. Su, K. Shimizu, A. Takeuchi, M. Uesugi, Damage micromechanisms of stress corrosion cracking in Al-Mg alloy with high magnesium content, Corros. Sci. 184 (2021), 109343, https://doi.org/10.1016/j.corsci.2021.109343.
[73] M.E. McMahon, Z.D. Harris, J.R. Scully, J.T. Burns, The effect of electrode potential on stress corrosion cracking in highly sensitized Al–Mg alloys, Mater. Sci. Eng. A 767 (2019), https://doi.org/10.1016/j.msea.2019.138399.
[74] M. Talianker, B. Cina, Retrogression and reaging and the role of dislocations in the stress corrosion of 7000-type aluminum alloys, Met. Trans. A 20 (1989) 2087–2092, https://doi.org/10.1007/BF02650294.
[75] M.L.C. Lim, R. Matthews, M. Oja, R. Tryon, R.G. Kelly, J.R. Scully, Model to predict intergranular corrosion propagation in three dimensions in AA5083-H131, Mater. Des. 96 (2016) 131–142, https://doi.org/10.1016/j.matdes.2016.01.089.
[76] D.R. Baer, C.F. Windisch, M.H. Engelhard, M.J. Danielson, R.H. Jones, J.S. Vetrano, Influence of Mg on the corrosion of Al, J. Vac. Sci. Technol. A: Vac., Surf., Films 18 (2000) 131–136, https://doi.org/10.1116/1.582129.
[77] J.H. Ai, M.L.C. Lim, J.R. Scully, Effective hydrogen diffusion in aluminum alloy 5083-H131 as a function of orientation and degree of sensitization, Corrosion 69 (2013) 1225–1239, https://doi.org/10.5006/0987.
[78] R.H. Jones, D.R. Baer, M.J. Danielson, J.S. Vetrano, Role of Mg in the stress corrosion cracking of an Al-Mg alloy, Met. Mater. Trans. A Phys. Met. Mater. Sci. 32 (2001) 1699–1711, https://doi.org/10.1007/s11661-001-0148-0.
[79] M.E. Mcmahon, P.J. Steiner, A.B. Lass, J.T. Burns, The effect of temper and composition on the stress corrosion cracking of Al-Mg alloys, Corrosion 73 (2017) 347–361, https://doi.org/10.5006/2317.
[80] M.E. Mcmahon, P.J. Steiner, A.B. Lass, J.T. Burns, The effect of loading orientation on the stress corrosion cracking of Al-Mg alloys, Corrosion 73 (2017) 713–723, https://doi.org/10.5006/2343.
[81] D. Tanguy, B. Bayle, R. Dif, T. Magnin, Hydrogen effects during IGSCC of pure Al-5Mg alloy in NaCl media, Corros. Sci. 44 (2002) 1163–1175, https://doi.org/10.1016/S0010-938X(01)00140-8.
[82] R.H. Jones, The influence of hydrogen on the stress-corrosion cracking of low-strength Al-Mg alloys, Jom 55 (2003) 42–46, https://doi.org/10.1007/s11837-003-0225-5.
[83] J.R. Pickens, J.R. Gordon, J.A.S. Green, The effect of loading mode on the stress-corrosion cracking of aluminum alloy 5083, Metall. Trans. A 14 (1983) 925–930, https://doi.org/10.1007/BF02644298.
[84] M.S. Bhuiyan, Y. Tada, H. Toda, S. Hang, K. Uesugi, A. Takeuchi, N. Sakaguchi, Y. Watanabe, Influences of hydrogen on deformation and fracture behaviors of high Zn 7XXX aluminum alloys, Int J. Fract. 200 (2016) 13–29, https://doi.org/10.1007/s10704-016-0092-z.
[85] H.K. Birnbaum, C. Buckley, F. Zeides, E. Sirois, P. Rozenak, S. Spooner, J.S. Lin, Hydrogen in aluminum, J. Alloy Compd. 253- 254 (1997) 260–264, https://doi.org/10.1016/S0925-8388(96)02968-4.
[86] R.K. Viswanadham, T.S. Sun, J.A.S. Green, Grain boundary segregation in Al-Zn-Mg alloys-implications to stress corrosion cracking, Met. Mater. Trans. A 11 (1980) 85–89, https://doi.org/10.1007/BF0270044.
[87] M.K. Tseng, H.L. Marcus, An investigation of the effect of gaseous corrosion fatigue on the J_{1C} of aluminum alloys, Scr. Met. 15 (1981) 427–430, https://doi.org/10.1016/0036-9748(81)90224-6.
[88] R.G. Song, M.K. Tseng, B.J. Zhang, J. Liu, Z.H. Jin, K.S. Shin, Grain boundary segregation and hydrogen-induced fracture in 7050 aluminium alloy, Acta Maler 44 (1996) 3241–3248, https://doi.org/10.1016/1359-6454(95)00406-8.